# Aerodynamically driven rupture of a liquid film by turbulent shear flow

Melissa Kozul [1,*] Pedro S. Costa [2,3] James R. Dawson [1] and Luca Brandt [1,3]

[1]*Department of Energy and Process Eng., NTNU, N-7491 Trondheim, Norway*
[2]*Faculty of Industrial Eng., Mechanical Eng. and Computer Science, 107 University of Iceland, Reykjavík, Iceland*
[3]*Linné FLOW Centre and SeRC (Swedish e-Science Research Centre), KTH Mechanics, SE-100 44 Stockholm, Sweden*

The rupture of a liquid film due to coflowing turbulent shear flows in the gas phase is studied using a volume-of-fluid method. To simulate this multiphase problem, we use a simplified numerical setup where the liquid film is "sandwiched" between two fully developed boundary layers from a turbulent channel simulation. The film deforms and eventually ruptures within the shear zone created by the coflows. This efficient setup allows systematic variation of physical parameters to gauge their role in the aerodynamically driven deformation and rupture of a liquid film under fully developed sheared turbulence. This work presents a detailed study of the developing pressure field over the deforming film and related aerodynamic effects, as previously suggested by other authors, in particular the role of the inviscid lift and drag forces. A cumulative lift force is introduced to capture the effect of the alternating pressure minima and maxima forming over the film, which amplify and eventually rupture the film. A velocity scale derived from the lift-induced drag force reflects the state of the turbulent boundary layer over the film and collapses the temporal development of this cumulative lift force as well as the amplitude of film deformation with some success for the different film thicknesses and Reynolds numbers.

## I. INTRODUCTION

Liquid fuel injection in the gas turbines of aircraft commonly utilize airblast atomization. This process exploits the kinetic energy of a flowing airstream to shatter the liquid fuel jet first into ligaments and then onward to drops [1]. Thus the breakup of a liquid film (also referred to as a liquid sheet or plane jet) is commonly demarcated into two phases: primary atomization, where a coherent liquid film disintegrates into ligaments and then drops, and secondary atomization, the breakup of liquid drops into yet smaller liquid drops [1,2]. Most modern airblast atomizers are of the prefilming type where, supplied from holes or slits upstream, the liquid fuel forms a thin film over the prefilming surface before being driven to the atomizing edge by turbulent flow. The use of a second air stream on the other side of the prefilmer to prevent fuel accumulation means that the breakup and eventual atomization of the liquid film occurs in the shear zone formed by the coflowing air streams [3], akin to a classical mixing layer. To maximize combustion efficiency and minimize pollutant production, the liquid fuel should be well atomized as quickly as possible as it enters the combustion chamber. This will promote evaporation and mixing in the gas phase resulting in stable,

---

*melissa.kozul@ntnu.no

low-emission combustion [1]. The current work seeks to pare down this complex physical problem to the core process of liquid sheet breakup under the effect of a turbulent sheared flow.

Many theoretical studies have investigated the shear-driven instability arising at the interface between a liquid film or sheet of finite thickness and a parallel-flowing gas. Given the symmetry of the problem about the central plane of the liquid, it is well-established that only two types of waves are possible at the surface of a flat liquid sheet at any given wave number within the linear stability framework that is mostly used. The first type considered is the antisymmetric (sinusoidal) mode where the two sheet surfaces are in phase, the second type being the symmetric (varicose, also called dilational) mode where the two sheet surfaces are out-of-phase. Squire [4] was the first to incorporate the effect of surface tension into analysis of the Kelvin-Helmholtz instability on the surface of an inviscid liquid sheet moving in an inviscid gas medium at rest, and to illustrate the competition between the two destabilization modes given the sheet's finite uniform thickness. It is therefore sometimes referred to as the Squire instability [5]. Reference [6] expanded the range of density ratios considered by previous authors to show that for low gas-to-liquid density ratios $\rho_g/\rho_\ell \ll 1$, the growth rate of the sinusoidal waves is larger than that of varicose waves, agreeing with previous results in the literature, yet finding additionally that, as the density ratio approaches unity, varicose waves become more unstable than sinusoidal ones. Earlier stability studies (e.g., [4,6]) focused on inviscid approaches to predict liquid sheet oscillation frequencies, wavelengths, and growth rates. Subsequently, Ref. [7] considered the temporally growing instabilities of a viscous liquid sheet within an inviscid gas. More recent efforts have accounted for the viscosity of both the liquid and surrounding gas phases (e.g., [8–10]), the inclusion of which generally improves predictions when compared to experimental work. However, the study [8] found that even when viscosity is considered, quantitative agreement is not satisfactory, indicating that the true phenomenon is more complex and probably beyond the capabilities of linear analysis. The same study also demonstrated the inherently three-dimensional nature of the atomization process, with active participation of transverse waves and longitudinal filaments. In addition to the primary streamwise Squire instability associated with a wavelength λ, considering the fragmentation of a slow liquid stream by a fast gas stream, Ref. [11] provided the theoretical basis for the subsequent destabilization of streamwise waves in the spanwise direction to form streamwise ligaments separated by a distinct wavelength $\lambda_\perp$. Due to the passage of the traveling primary undulations, fluid particles in the slow stream are periodically accelerated perpendicular to the interface. The resulting accelerations of the liquid interface perpendicular to its surface rapidly become large enough (much larger than the acceleration due to gravity in the laboratory [11]) to produce a secondary Rayleigh-Taylor instability. The numerical study [10] concluded that the length scale of the most unstable mode in the linear regime is too small to fragment the entire liquid sheet and that it therefore cannot be directly responsible for its atomization. By considering the spectrum of surface wavelengths preceding primary atomization, they found that standard linear theories tend to underestimate the dominant length scales associated with atomization by approximately two to three orders of magnitude, constituting a serious discrepancy from their volume-of-fluid (VOF) simulations. It was emphasized in Ref. [10] that their numerical results displayed good agreement with linear theories during the initial development of interfacial instabilities within the linear regime. Nevertheless, they showed that these dominant modes were clearly not the ones responsible for atomization. The authors point instead to the emergence of a much larger mode following the linear window, with a wavelength approximately an order of magnitude larger than the most unstable wavelength predicted in the linear regime, as being that which eventually causes breakup. Initial (linear) instabilities do lead to the breakup of a small portion of the liquid sheet (i.e., the bottom and top surfaces), however due to their small magnitude, these instabilities leave the liquid core intact and therefore do not directly lead to atomization of the sheet. In a subsequent study of a liquid jet [12], it was confirmed that, while the most unstable modes are captured in the simulations and agree with theoretical predictions, these modes were once again found not to be directly responsible for fragmenting the liquid core or causing primary atomization. Their action is limited to stripping off

the surface of the liquid jet, while its liquid core remained intact for another 20 nozzle diameters downstream.

For turbulent shear flows over liquid films leading to breakup, experiments are largely confined to observations of the disintegrating sheet to determine breakup length (e.g., [13,14]), documentation of liquid sheet topology, as well as determining broad breakup processes or regimes. Reference [15] measured streamwise growth rates of waves within liquid sheets with coflowing uniform air by systematically forcing the sheet upstream at a range of frequencies. There has additionally been a heavy focus on measurements of the liquid particle diameter far downstream once the sheet has atomized [16]. The phenomenological study in [14] measured the frequency of an oscillating sheet as well as breakup length deduced from experimental photographs. The chief experimental difficulty in investigating the primary breakup phase lies in obtaining an accurate description of the flow field across the gas-liquid interface. More recently, novel interfacial velocimetry techniques have been developed [17,18] allowing observation of primary breakup, where laboratory measurements have typically been restricted to secondary breakup, which shows more generality. Reference [18] found the aerodynamic stress $\tau_g = \rho_g U_g^2$, where $\rho_g$ is the gas density and $U_g$ is the mean gas velocity, to be an important quantity governing primary breakup. The study emphasized the phenomenon of accumulation breakup, where the liquid sheet always disintegrates at the edge of the atomizer, and it closely investigated different breakup sequences. The experimental study of Ref. [19] created a regime map delineating liquid sheet breakup into three different regimes ("smooth," "waves," "accumulation") depending on operating conditions, and it developed a correlation between breakup length and film thickness. The experiment of Ref. [20] injected a water jet coaxially into a high-velocity gas jet, and increased the air turbulence while maintaining the mean air velocity, finding increased lateral motion to be the most obvious visual effect. The authors found jet dynamics to be less symmetric, with a shortened breakup length and more complex liquid ligament shapes. Moreover, Ref. [20] understood the breakup mechanism under high turbulence intensity to be driven by "overturning" of the liquid jet, which leads to liquid perpendicularly aligned with the gas stream, resulting in strong normal forces that "blow up" the liquid to generate thin membranes that then proceed to secondary breakup. The experiments of Ref. [21] investigated the role of shear-driven gas-phase turbulence on the primary atomization and breakup morphology of nonturbulent liquid jets. They found the ratio of the turbulent Weber number to the mean Weber number to be a relevant parameter, as was the turbulence intensity, in dictating the primary breakup length. An alternate breakup regime was described by the experimental study of Ref. [22] where the emergence of cellular structures was considered as being the dominant rupture mechanism of the sheet. The emerging "cells" in the deforming liquid sheet, presumably related to the secondary spanwise destabilization [11], were described as comprising thin films of a higher amplitude surrounded by ligaments of a lower amplitude.

Given the limitations of laboratory measurements and theoretical modeling, numerical simulations are well-placed to make a substantial contribution, particularly in the primary breakup stage. The rapid development of multiphase simulation methods combined with increasing computing power means that interface capturing simulations of multiphase flows within the fully turbulent regime are now feasible to capture the three-dimensionality and unsteadiness of realistic flows. Recently, simulations have been conducted of a semirealistic film breakup system [23] including a splitter plate, with a turbulent gas only on one side of the film and a prescribed error function profile for the gas-phase velocity over the liquid film to model the boundary layer coming off the splitter plate. This study investigated the grid resolution necessary to faithfully capture downstream development of terms in the kinetic energy budget and the smallest size of droplets formed in atomization, finding converged results of the turbulent dissipation only with the finest mesh they used. They found agreement with linear stability theory both in the dominant frequency for the wave formation, deduced from spectra of the interfacial height near the edge of the splitter plate where wave amplitudes remain small, as well as in the exponential growth in the mixing layer thickness for an intermediate distance downstream of the splitter plate. They reported that simulation results deviated from linear theory as the amplitude of the interfacial wave grows and propagates

downstream and nonlinear effects become important. Despite making approximations, this study required a costly numerical setup where it may be unfeasible to perform parametric studies to investigate the influence of flow parameters and material properties. Another recent numerical study used a similar setup including a splitter plate [24], once again imposing a turbulent gas only on one side of the film, and investigated the role of turbulence by superimposing different intensities of disturbances on the error function profiles for the mean streamwise inlet gas velocity. The authors compared their numerical results to predictions of linear stability analysis incorporating a simple turbulent eddy viscosity model, and they found that while linear theory was able to capture the trend of increasing dominant frequency and spatial growth rate with increasing gas inlet turbulence intensity, it significantly underestimated the values themselves. Given the wide range of scales involved in the whole atomization process, the numerical framework of Ref. [25] seeks to mitigate simulation costs by introducing an intermediate modeling scale, whereby the medium liquid drops produced by primary breakup are represented as rigid spheres fully coupled to the two-phase field. This methodology thus attempts to bridge the scale gap between the coupled level-set/volume-of-fluid method (CLSVOF), adequately capturing the primary breakup stage, and the particle tracking algorithm used to represent fine spray dynamics. The recent work of [26] demonstrates an alternate approach to control the computational resources required for this demanding physical problem by using a direct numerical simulation (DNS) of the flow in the vicinity of the splitter plate embedded within a larger large-eddy simulation (LES) to simulate a realistic turbulent nozzle flow. This was compared with a steady boundary layer flow as used in previous numerical studies. The study found the Sauter mean diameter (SMD) of the spray was reduced by almost 20% if the turbulence was taken into account, demonstrating that the turbulent scales in the gaseous flow increase the proportion of fine droplets.

Quantifying the forces acting on a liquid film requires access to the pressure field, which is difficult, if not impossible, to deduce experimentally, yet the enhancement of liquid structure breakup through the aerodynamic lift effect has been previously suggested [2,27], underlining the potentially key role of aerodynamic forces in atomization. It is well understood that, for $\rho_\ell / \rho_g < 500$, aerodynamic effects greatly influence liquid breakup [27], this ratio being on the order of 100 for aircraft engines [2]. Unlike in laboratory experiments of this physical problem, the present simulations have full access to the velocity and pressure fields. We will therefore directly investigate predominantly inviscid aerodynamic effects previously only suggested by other authors, our focus being on large film deformations beyond the linear regime that directly result in film rupture. To do this, we consider a simplified numerical setup using a recently developed VOF method [28]. A stationary liquid film is sandwiched between fully developed sheared turbulent gas flows from a precursor simulation of a turbulent channel flow. This setup allows us to systematically vary parameters such as film thickness and turbulent gas flow Reynolds number to gauge the effect upon momentum transfer into the initially stationary liquid film. Aerodynamic quantities such as lift and lift-induced drag are considered to describe the film while it is still intact. The recent simulations of Ref. [29] utilized a similar "sandwich" setup but prescribed initial interfacial perturbations, for example a sinusoidal surface on a liquid film, as did Ref. [30]. The numerical study of Ref. [31] place a liquid sheet between homogeneous isotropic turbulence with no liquid or density jumps. The authors demonstrated that, even in the absence of mean shear, turbulence will provoke primary breakup in a liquid sheet if the Weber number is high enough, therefore suggesting the importance of realistically representing the gas-phase turbulence. There has been a keen focus on primary instabilities and minute topological changes [2,29], whereas the present work seeks to investigate the influence of aerodynamic effects and material properties on global phenomena such as deformation amplitude and time to breakup. This numerical setup using mirrored turbulent channel velocity fields is both simple and effective. The present technique considers a more realistic turbulent gas phase acting directly on the liquid surface without predetermined surface perturbations or introduced scales, aiming to understand how the large deformations of the liquid film leading to rupture arise spontaneously from the turbulence-laden gas phase, as they do in practical engineering applications.

## II. MATHEMATICAL FORMULATION

The present simulations use a recently implemented VOF method for multiphase flow simulations [28,32]. This interface-capturing approach has the major strength of ensuring mass conservation by construction, a property particularly desirable for the present physical problem since statistics will be collected over a considerable simulation time. Hereafter, we refer to fluctuating velocities $u$, $v$, and $w$ in the $x$-streamwise, $y$-wall- or film-normal, and $z$-spanwise directions. In that which follows, the subscript $g$ will refer to the turbulent gas phase, and subscript $\ell$ to the liquid phase, representing the initially quiescent film. The following is a summary of the formulation presented in Ref. [32]. The gas-liquid (two-fluid) motion is governed by the conservation of momentum and the incompressibility constraint. Additionally, the kinematic and dynamic interactions between the two fluid phases are determined by enforcing continuity of the velocity at the interface between the two phases:

$$\mathbf{u}^\ell = \mathbf{u}^g, \tag{1}$$

and imposing the following surface stress boundary condition at the interface [33]:

$$\sigma^\ell \cdot \mathbf{n} = \sigma^g \cdot \mathbf{n} + \gamma \kappa \mathbf{n}, \tag{2}$$

where $\sigma = \sigma_{ij}$ is the Cauchy stress tensor, $\mathbf{n}$ is a vector normal to the interface, $\kappa$ is the interface curvature, and $\gamma$ is the surface tension coefficient, assumed to be constant in the present formulation. The VOF method following Ref. [28] is used to numerically solve the two-phase flow problem. An indicator (or color) function $H$ is introduced to identify each phase, in the present methodology $H = 1$ within the liquid phase, and $H = 0$ within the gas phase. $H$ is updated according to the following advection equation:

$$\frac{\partial \phi}{\partial t} + \nabla \cdot (\mathbf{u} H^{\mathrm{ht}}) = \phi \nabla \cdot \mathbf{u}, \tag{3}$$

where $\mathbf{u}$ is the local fluid velocity and $\phi$ is the cell-averaged value of the indicator function $H$. $H^{\mathrm{ht}}$ is the hyperbolic tangent function approximating the indicator function $H$, which is determined along with the curvature $\kappa$ and the surface normal vector $\mathbf{n}$ via the multidimensional tangent of hyperbola for interface capturing (MTHINC) method [28]. Since we have set $\phi$ to be the cell-averaged volume fraction of the liquid, $\phi = 1$ if a cell is fully filled with the liquid phase, $\phi = 0$ when only gas fills the cell, and $0 < \phi < 1$ at the diffuse interface. Once $\phi$ is known, the two-fluid equations may be written in the so-called one-continuum formulation, meaning only one set of equations is solved over the entire computational domain. Thus the single velocity vector $\mathbf{u}$ field is defined everywhere, governed by the following equations:

$$\rho \left( \frac{\partial \mathbf{u}}{\partial t} + \mathbf{u} \cdot \nabla \mathbf{u} \right) = -\nabla p + \nabla \cdot \mu (\nabla \mathbf{u} + \nabla \mathbf{u}^T) + \gamma \kappa \mathbf{n} \delta, \quad \nabla \cdot \mathbf{u} = \mathbf{0}, \tag{4}$$

and it is deduced by applying a volume averaging procedure, where $p$ is the pressure, $\rho$ is the density, $\mu$ is the dynamic viscosity, and $\delta$ is the Dirac delta function at the interface of the two fluids. The density $\rho$ and dynamic viscosity $\mu$ are defined as mixed forms:

$$\rho = \phi \rho^\ell + (1 - \phi) \rho^g, \qquad \mu = \phi \mu^\ell + (1 - \phi) \mu^g. \tag{5}$$

## III. NUMERICAL METHODOLOGY

Figure 1 shows how the initial velocity fields for the VOF simulations are prepared. The velocity fields are from a fully developed turbulent channel flow with walls at the top and bottom of the domain, simulated using a single-phase channel solver [34]. Table I summarizes the numerical parameters of the channel simulations. Split at the channel centerline, the fully developed fields are inverted in the wall-normal (or film-normal) direction $y$ and the liquid film placed between the turbulent shear layers in the $xz$-plane to form the "sandwich" setup.
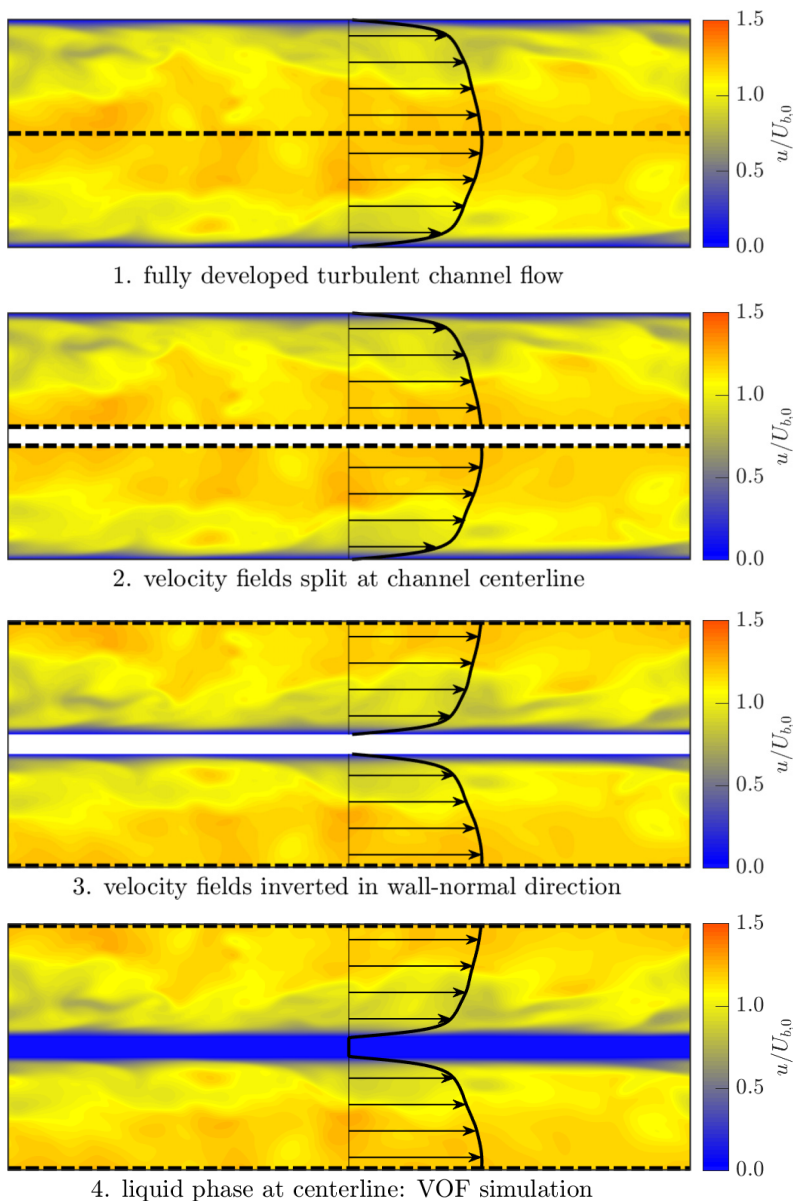
FIG. 1. Four-step method to set up the VOF simulations: use of velocity fields from fully developed turbulent channel flow simulations. Shown here are contours of the streamwise velocity; however, the procedure is applied to all three velocity components to form the starting fields of the VOF simulations. The thick black contour indicates the initial mean streamwise velocity profile. Dashed lines indicate how a single plane at the centerline is recast as a periodic boundary condition, meaning the flow field is still numerically contiguous in the "sandwich" VOF setup.

Table II summarizes the parameters of the liquid film simulations, where subscript 0 refers to parameters at the instant the film simulations are started. The VOF is set to 1 in the region between the inverted shear layers, and 0 elsewhere. The initial velocity is 0 within the film "sandwiched" between the inverted shear layers to model the action of fully developed wall-bounded turbulence on the gas-liquid interface on both sides of the film. Reference [35] found that the liquid boundary

TABLE I. Parameters for the channel simulations used to form the turbulent gas phase in the multiphase simulations. Both channel simulations have a domain size $L_x/h = 6$, $L_z/h = 3$, where $h$ is the channel half-height. A constant grid spacing was used in all three dimensions. Superscript "+" indicates viscous scaling (e.g., $\Delta x^+ = \Delta_x u_\tau / \nu_g$).

| $\mathrm{Re}_b$ | $\mathrm{Re}_\tau$ | $N_x$ | $N_y$ | $N_z$ | $\Delta x^+$ | $\Delta y^+$ | $\Delta z^+$ |
|---|---|---|---|---|---|---|---|
| 5600 | 180 | 1152 | 384 | 576 | 0.94 | 0.94 | 0.94 |
| 13750 | 393 | 2496 | 832 | 1248 | 0.94 | 0.94 | 0.94 |

layer does not play an important role in the gas-liquid interface interaction. The resulting periodic boundary condition from the inverted channel fields is exploited at the top and bottom of the domain. That is, flow that was contiguous at the centerline is now contiguous via the periodic boundary condition. Periodic boundary conditions are also used in the streamwise and spanwise directions, and no flow forcing is applied once the film simulations are started. The present cases are therefore temporal simulations. In analogy to the spatial system of the physical prefilmer, when the VOF simulation is launched, the flow is a model for that at the edge of the atomizer as the fuel film leaves the atomizing edge. The flow's development in time is then analogous to that of the flow as it moves away from the atomizing edge of the prefilmer in the spatial system, where the mean shear of the gas phase decays in the streamwise direction. The initial condition thus formed inherently respects the boundary conditions of the physical problem, ensuring that the initial condition rapidly adapts to the full multiphase flow problem. Numerical artefacts due to adjustments of the flow to the initial condition are thus rapidly mitigated.

This numerical setup permits systematic variation of parameters known to play an important role in the liquid film's primary breakup, such as the film thickness and the Reynolds number of the turbulent gas phase (effectively, the initial shear stresses felt by the surface of the film, which had been at the walls in the channel flow simulations). Liquid-to-gas density and viscosity ratios are $\mu_l/\mu_g = \rho_l/\rho_g = 40$. The initial Weber number is set as $\mathrm{We}_0 = \rho_l U_{b,0}^2 w_{l,0}/\gamma = 500$ (note that since our liquid is initially at rest, the present Weber number is defined solely in terms of the gas-phase velocity), where $U_{b,0}$ is the bulk velocity of the channel flow, $w_{l,0}$ is the initial film thickness, and $\gamma$ is the surface tension coefficient, as a direct comparison to previous numerical work [2]. An alternate, temporally developing Weber number based on the streamwise wavelength of the film's deformation will be considered in Sec. IV C [Fig. 9(d)]. Three film thicknesses are considered (suffixes to case names "thin," "med," and "thick" refer to the physical thickness $w_{\ell,0}$ scaled by the channel simulation half-height $h$). The role of the Reynolds number is presently investigated in a limited sense with one of the cases using a turbulent gas phase at a higher starting Reynolds number of $\mathrm{Re}_{\tau,0} = 393$ (HiRe-thin); all other cases begin with a turbulent gas phase at $\mathrm{Re}_{\tau,0} = 180$.

TABLE II. Parameters for the liquid film simulations. Subscript "0" refers to parameters when the film simulations are started. Fully developed turbulent velocity fields from the channel simulations (Table I) form the gas phase; $\mathrm{Re}_{\tau,0}$ refers to their steady-state Reynolds number. The viscous-scaled initial film thickness is $w_{\ell,0}^+ = \mathrm{Re}_{\tau,0}(w_{\ell,0}/h)$. $(N_{\ell,y})_0$ is the number of grid points over the liquid phase at the start of the VOF simulations. All simulations have domain size $L_x/h = 6$, $L_y/h = 2 + w_{\ell,0}$, $L_z/h = 3$.

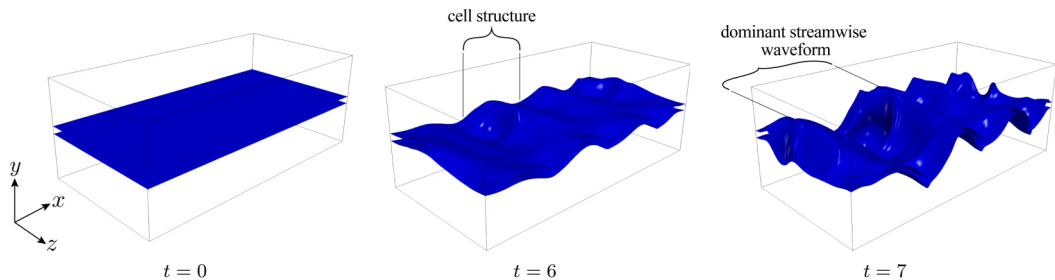| Case name | Symbol | $\mathrm{Re}_{\tau,0}$ | $w_{\ell,0}/h$ | $w_{\ell,0}^+$ | $N_x$ | $(N_{\ell,y})_0$ | $N_y$ | $N_z$ | $(\Delta x^+)_0$ | $(\Delta y^+)_0$ | $(\Delta z^+)_0$ |
|---|---|---|---|---|---|---|---|---|---|---|---|
| LoRe-thin | ● | 180 | 1/12 | 15.0 | 2304 | 32 | 800 | 1152 | 0.47 | 0.47 | 0.47 |
| LoRe-med | ▲ | 180 | 1/6 | 30.0 | 1152 | 32 | 416 | 576 | 0.94 | 0.94 | 0.94 |
| LoRe-thick | ■ | 180 | 1/3 | 60.0 | 1152 | 64 | 448 | 576 | 0.94 | 0.94 | 0.94 |
| HiRe-thin | ● | 393 | 1/13 | 30.4 | 2496 | 32 | 864 | 1248 | 0.94 | 0.94 | 0.94 |

FIG. 2. Visualization of the surface of the liquid film (contours drawn at $\phi = 0.5$) for the LoRe-med case in time. The initially flat film deforms under the action of the fully developed turbulent gas-phase boundary layers.

A uniform grid is used in all three dimensions, with grid spacing $\Delta x_0^+ = \Delta x\, u_{\tau,0}/\nu_g = \Delta y_0^+ = \Delta z_0^+ < 1$, where $u_{\tau,0}$ is the steady-state friction velocity of the gas phase from the channel simulations, and $\nu_g = \nu_l$ is the gas phase kinematic viscosity. The adequacy of the grid resolution, a contentious topic in multiphase simulations [2], was investigated with a companion simulation to LoRe-thin named "LoRe-thin-loRes" using a coarser grid than that of LoRe-thin (see the Appendix), equivalent to the grid resolution used herein for the other cases of Table II. A high level of similarity was found between the two thin-film simulations with different resolutions, although some differences emerge once the film ruptures, since topology changes in VOF methods occur when liquid structures approach the grid size [36]. Therefore, the lower resolution is found to be satisfactory for capturing the film's deformation while still intact, being the route to rupture, which is the concern of the present work. We note that the "thin" film case is the most demanding since we can expect smaller liquid phase features to arise for thinner liquid films. This suggests that if the resolution is shown to be adequate for the thin film, this same resolution will be satisfactory for thicker films (i.e., the LoRe-med and LoRe-thick cases). Unless otherwise stated, simulation times cited throughout this work are normalized by $U_{b,0}/(2h)$. A constant time step $\Delta t = 10^{-4}$ is used for all cases herein, being smaller than that suggested by Eq. (99) in Ref. [37].

## IV. RESULTS

### A. Visualizations

In this section, we consider important physical features of the liquid film's deformation and rupture, and we establish some commonalities with experimental work in the literature. A first view of the physical problem is given in Fig. 2, where the surface of the liquid film is shown as it deforms during the simulation of the LoRe-med case. We see that there is a considerable time delay until significant deformations of the film emerge at $t = 6$, which then rapidly grow until the film is at the point of rupture by $t = 7$. In addition to a dominant waveform in the streamwise direction, there are secondary "cells" forming across the span reminiscent of that seen in the experiments of Ref. [22] for water films subject to turbulent air coflows. A cellular structure with thickening edges clearly emerges at $t = 6$ in Fig. 2. Secondary spanwise destabilizations (transverse modulations) have been observed experimentally, even in the absence of gas-phase turbulence [11,38–40]. The emergence of a spanwise wavelength $\lambda_\perp$ was attributed to the periodic acceleration of fluid particles in the slow stream perpendicular to the interface due to the passage of the traveling streamwise primary undulations, resulting in a "passive" (i.e., not requiring turbulence) secondary Rayleigh-Taylor instability [11]. Figures 3 (at time $t = 1$) and 4 (at time $t = 4$) plot the cell-average volume fraction of the liquid $\phi$ and the streamwise velocity fields in the $xy$-plane for three of the present cases. This permits a first visual comparison between the LoRe-thin and LoRe-med cases, both with starting gas phase friction Reynolds number $\mathrm{Re}_{\tau,0} = 180$, and the HiRe-thin case, with $\mathrm{Re}_{\tau,0} = 393$.
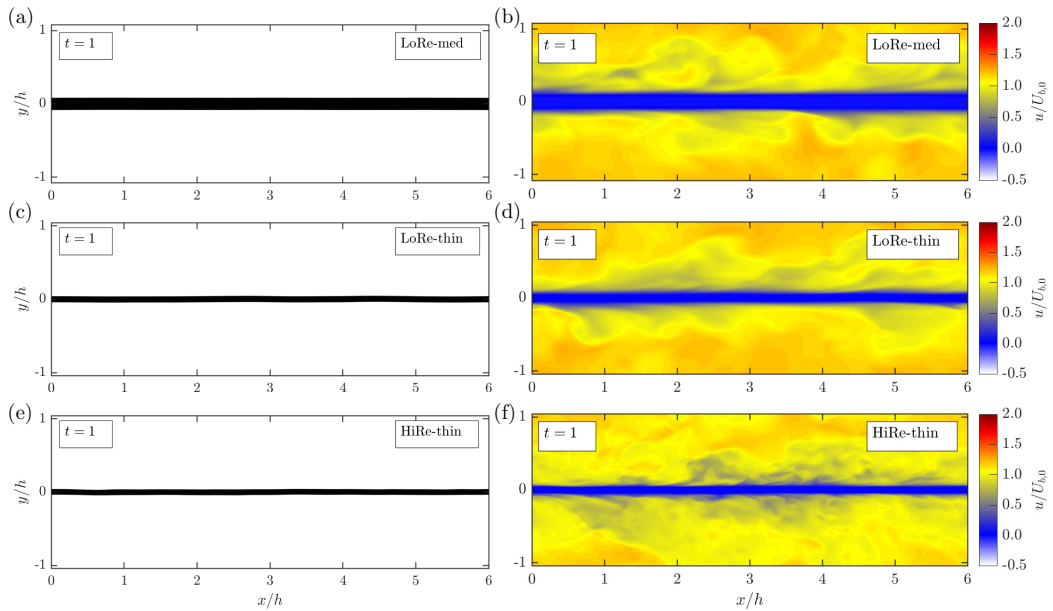
FIG. 3. Visualizations of three cases of the VoF simulations at $t = 1$, fields of the "sandwich" film setup at an early time. Top: LoRe-med case; middle: LoRe-thin case; bottom: HiRe-thin case. Left: the cell-averaged volume fraction of the liquid, $\phi$; right: streamwise velocity fields. Bulk velocity is to the right.
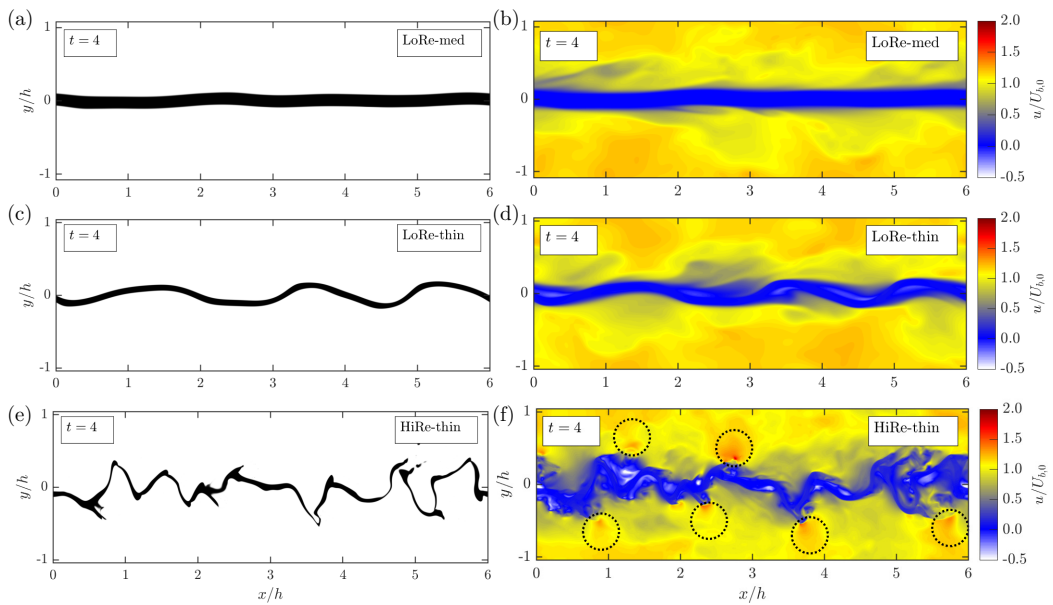


FIG. 4. Visualizations of three cases of the VOF simulations at $t = 4$. Top: LoRe-med case; middle: LoRe-thin case; bottom: HiRe-thin case. Left: the cell-averaged volume fraction of the liquid, $\phi$; right: streamwise velocity fields. Dotted circles in (f) mark regions of high streamwise velocity. Bulk velocity is to the right.

The initially flat film (Fig. 3) is deformed by the fully developed turbulent boundary layers on either side of it after some time at $t = 4$ (Fig. 4). As expected, a thicker film is more resistant to deformation as only small perturbations are present in the LoRe-med case at $t = 4$. On the other hand, the LoRe-thin case is highly sinusoidal by this time, whereas the HiRe-thin case is much more contorted by $t = 4$, suggesting nonlinear development, and it has in fact already ruptured. The influence of the Reynolds number is clearly significant, increasing the deformation and contortion, which results in rupture. At higher Reynolds number, a wider spectrum of scales interacts with the film, as is clear from Fig. 3(f), since $w_{\ell,0}/\delta_\nu$ is larger, where $\delta_\nu = \nu/u_\tau$ is the viscous wall unit. Additionally, liquid ligaments can be seen to be "peeling" from the bulk of the liquid by $t = 4$ in Fig. 4(e). These events directly precede film rupture and were found to cause the ensuing rupturing mechanism first identified by Ref. [17]. By $t = 4$ in Figs. 4(d) and 4(f), some reversed flow (in white) appears for both the LoRe-thin and HiRe-thin cases. For the HiRe-thin case, these high-speed regions forming over alternating extrema [highlighted with dotted circles in Fig. 4(f)] are especially pronounced given the film's high contortion. Figure 4 demonstrates the sensitivity of the rate and nature of film deformation to the turbulence in the gas phase and therefore the necessity of realistically representing gas-phase turbulence in numerical studies of this physical problem.

Qualitatively, similar behavior has been observed in experimental investigations. Reference [41] found that for velocity and momentum ratios for which the sinusoidal mode is dominant, liquid sheet oscillation can cause air boundary layer separation at the interface for the wave troughs. The authors postulated that this separation causes a pressure difference on both sides of the liquid sheet, which can be partly responsible for enhancement of the flapping motion. They also found that before breaking, the sheet oscillations grow nonlinearly and the sinusoidal wave deforms into a "zigzag" shape, as observed for the HiRe-thin case in Fig. 4(f). The peaks then bend and point upstream, forcing the air to recirculate. They hypothesized that these recirculation zones may act as a feedback mechanism contributing to increasing wave growth. The semirealistic simulations of Ref. [23] also reported that the increasing interfacial wave amplitude in their mixing layer between parallel gas and liquid streams acts as an obstacle to the gas flow, causing the flow to separate at the downstream face of the wave, giving rise to a turbulent wake. The cellular rupture phenomenon in air-blasted liquid sheets was investigated experimentally by Ref. [22], where they systematically studied the effect of both the turbulent air and liquid (water) sheet velocity. They found that turbulent transition of the liquid jet did not have any noticeable effect on cellular structures and the ensuing sheet breakup, with similar results for similar relative gas-liquid velocities. They deduced the size of the "cell" structures in the disintegrating sheet to vary approximately as $U_r^{-2}$, where $U_r$ is the relative velocity between the gas and liquid phases. In the present cases, the bulk velocity is the same in all cases, yet smaller "cell" structures form for the HiRe-thin case in Fig. 4 due to the higher Reynolds number. We have shown here that our temporal VOF simulations are qualitatively reflective of experimental work on this same physical problem. Our continuing analysis is inspired by phenomena such as the reversed and high-speed flow regions in particular, and we will use ideas from classical aerodynamics.

### B. Temporal development

Figure 5 plots various profiles averaged in the homogeneous $xz$-planes (the initial plane of the film) following that shown in Ref. [2] for the liquid turbulent jet within a quiescent gas phase. The curves pertain to the same cases as those shown in Figs. 3 and 4. This permits a more quantitative appraisal of the average evolution of the fields in time and the differing rates of evolution between the cases. The curves are colored by time, such that the same color in each subfigure corresponds to the same development time in bulk units after the VOF simulations are started for each case.

The plane-averaged volume fraction of the liquid $\phi$ is shown in Figs. 5(a)–5(c). The starting steplike profile of $\overline{\phi}$ is gradually smeared out as the film deforms, moving fluid away from the centerline. This happens at a markedly different rate for the different cases. The value $\overline{\phi}$ at the centerline reduces from the starting $\overline{\phi} = 1$ to $\overline{\phi} \approx 0.5$–$0.6$ at $t = 6$ for the LoRe-med case, at $t = 4$
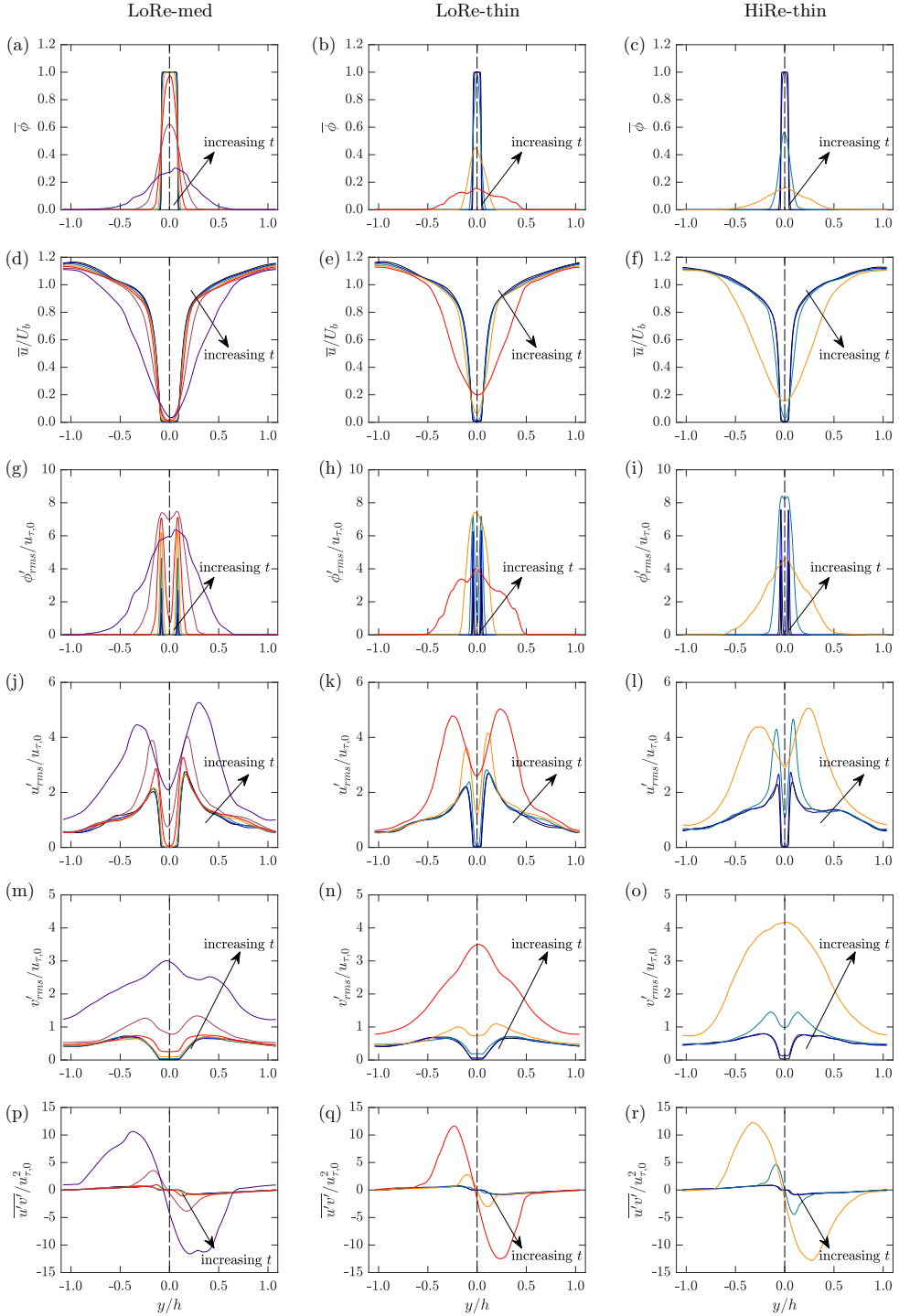
FIG. 5. Statistics deduced by averaging in the homogeneous $xz$-planes; left column: LoRe-med case, $\mathrm{Re}_{\tau,0} = 180$ ($w_{\ell,0}/h = 1/6$); middle column: LoRe-thin case, $\mathrm{Re}_{\tau,0} = 180$ ($w_{\ell,0}/h = 1/12$); right column: HiRe-thin case, $\mathrm{Re}_{\tau,0} = 393$ ($w_{\ell,0}/h = 1/13$); curves colored by time: ———, $t = 1$; ———, $t = 2$; ———, $t = 3$; ———, $t = 4$; ———, $t = 5$; ———, $t = 6$; ———, $t = 7$; – – –, domain centerline.

for the LoRe-thin case, and at $t = 3$ for the HiRe-thin case. As seen above in the visualizations, both a thinner film and a higher gas-phase Reynolds number serve to increase the momentum transfer to the liquid phase increasing the rate of the liquid's spread away from the centerline. Despite different temporal evolutions, the qualitative trends appear to be similar among the cases, that is, the liquid phase is spread in a similar manner throughout the domain in a mean sense. Figures 5(d)–5(f) show the development of the mean streamwise velocity. Changes to the boundary layer profiles are due to both momentum transfer to the liquid sheet (i.e., significant flattening of $\overline{\phi}$) and, likely to a smaller extent, dissipation in the gas phase, since there is no flow forcing in the VOF simulations. Figures 5(g)–5(i) show the root-mean-squared (rms) fluctuations in $\phi$. At the start of the VOF simulations, $\phi'_{\text{rms}}$ is zero everywhere since the film is initially perfectly quiescent. Regions of nonzero $\phi'_{\text{rms}}$ are only found near the film surface at early times, resulting in two sharp peaks about the centerline. After some time, fluctuations in $\phi$ are felt through the whole thickness of the film, and at later times spread away from the centerline as the film deformations grow. Reference [42] conducted spatial large-eddy simulations of planar air/water air-blast atomization, and found similar development in the rms fluctuations within the liquid phase at positions downstream of the splitter plate, although their incoming gas phase was not turbulent.

Figures 5(j)–5(o) show how the streamwise and spanwise velocity fluctuations evolve throughout the domain. Note that they were also zero within the film at $t = 0$ yet increase through the liquid phase as the film deforms. The initial peak values in both streamwise and film-normal velocity variance are amplified in time by the film's deformation. The streamwise velocity fluctuations $u'_{\text{rms}}$ remain double-peaked across the film even at late times, with the strongest fluctuations occurring at the film's surface on either side. The film-normal velocity fluctuations, however, tend to evolve such that there is a single peak roughly at the film's centerline. A large and sudden increase in the Reynolds stresses both through and about the film's edge is seen in Figs. 5(p)–5(r) as significant momentum is transferred from the gas phase into the liquid film. Again the final profiles are very similar among the different cases, yet they occur at different times. The film thickness and gas-phase Reynolds number, therefore, both have a role in determining the rate of film deformation and rupture.

### C. Quantifying the deforming film surface

Fig. 6 shows contours of the film surface as a deviation from the original film location, referred to as surface displacement $\zeta$ by analogy with that used in a wind-driven wave context (e.g., Ref. [43]). Contours of $\zeta$ are shown in the $xz$-plane (being the plane of the initial film), computed with the aid of a reconstructed level-set field [44], and scaled with the initial film thickness $w_{\ell,0}$. At early times, deformations are small and incoherent, although their sizes show Re dependence, and they are due to the shear stresses and pressure fluctuations of the turbulent gas-phase boundary layer over the film's surface (which had developed over a solid wall in the channel simulations). Such deformations by a turbulent wind on a liquid surface, below the onset of wave generation, appear similar to the "wrinkles" in the wind-driven wave study of Ref. [45]. At later times, a clear waveform in the streamwise direction emerges as the deviations from the original film location increase. These large deformations are those that eventually rupture the film. It is also interesting to compare the spanwise extent of this dominant streamwise waveform. In the LoRe-med and LoRe-thin cases, a single streamwise waveform extends over the whole span, whereas the film's surface in the HiRe-thin case is more three-dimensional, although a clear waveform in the streamwise direction nonetheless emerges. A weaker spanwise waveform is also evident, as seen at later times in Fig. 2 for the LoRe-med case and giving rise to "cell" structures as previously reported [22]. A similar progression from disordered small surface displacements to large ordered streamwise waves was also observed for the surface of wind-wave generation in the numerical study of deep-water waves in Ref. [46].

Figure 7 plots the temporal development of spectra of the surface displacement as a function of streamwise wave number $k_x$ and spanwise wave number $k_z$. The maximum is marked by a red bullet
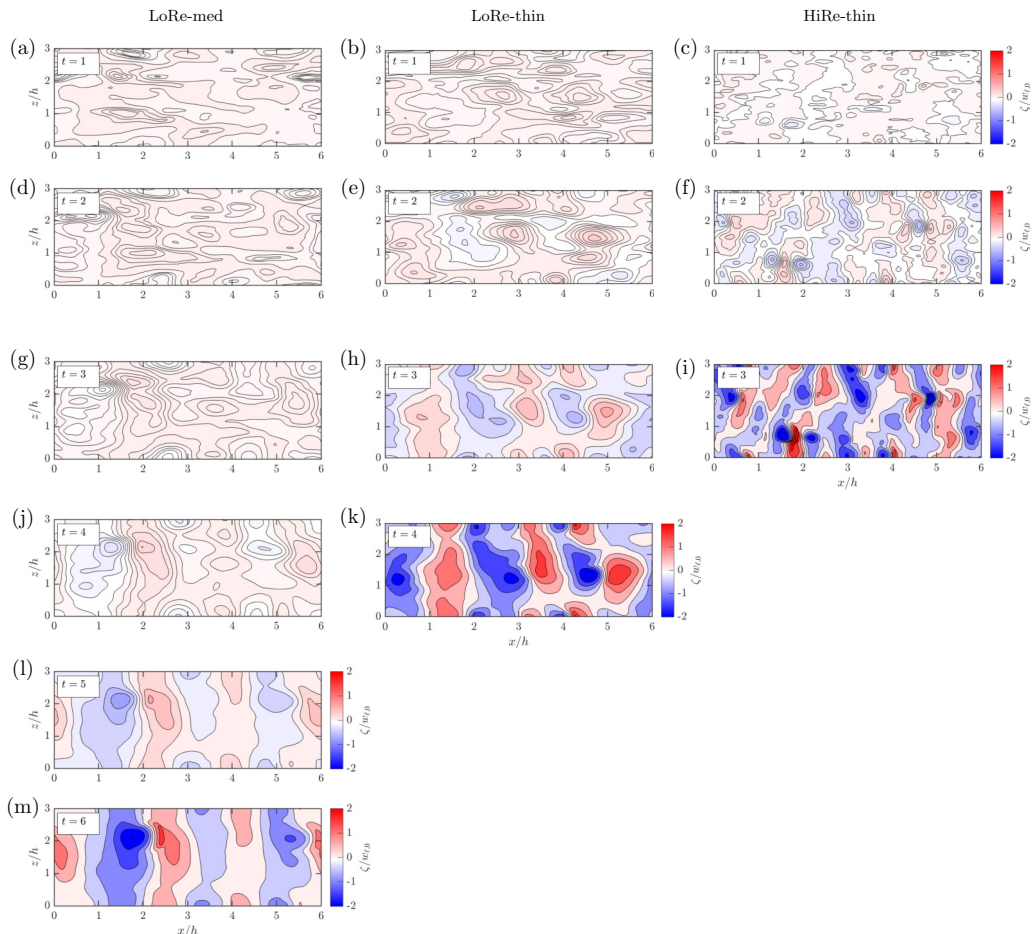
FIG. 6. Contours of the deforming (top) film surface displacement $\zeta$ for the same three cases shown in Figs. 3, 4, and 5, scaled by initial film thickness $w_{\ell,0}$. Time advances downward in each column for each case. Contours are similar for the bottom film surface (not shown).

in each subfigure. The spectra are mostly rounded up to $t = 2$, reflecting the early random surface displacements (Fig. 6). At times $t \gtrsim 3$, the highest-energy contour of the spectra becomes elongated along the $k_x$ axis, although there is still significant energy along the spanwise $k_z$ axis, reflecting the secondary spanwise waveform seen in Fig. 6 at late times. A peak for small $k_x$ emerges for the LoRe-med (at $t = 6$) and HiRe-thin cases (at $t = 3$), similar to that seen in the spectra of surface displacements for the deep-water wave simulations of Ref. [46]. It is centered at a larger $k_x$ for the HiRe-thin case indicating the smaller size of the emerging dominant streamwise waveform (and Reynolds number dependence on $k_x$).

Several previous studies have attempted to measure the amplitude and wavelength of a deforming liquid surface. Reference [47] extracted binary images of an atomizing liquid jet to deduce wavelengths ($\lambda$) and amplitudes ($a$) while the liquid core was still intact. An analysis based on the local maxima and minima of the film surface extracting the streamwise $\lambda$ and $a$ is undertaken for the present cases. Figure 8 shows contours of the film's surface in the $xy$-plane for several of the present cases making the emerging streamwise wavelength clear. The cases are approximately sinusoidal, although LoRe-thick in Fig. 8(c) shows a varicose-like mode as slight film thickening is observed. Figure 8 also indicates local maxima (red open bullets) and local minima (blue open
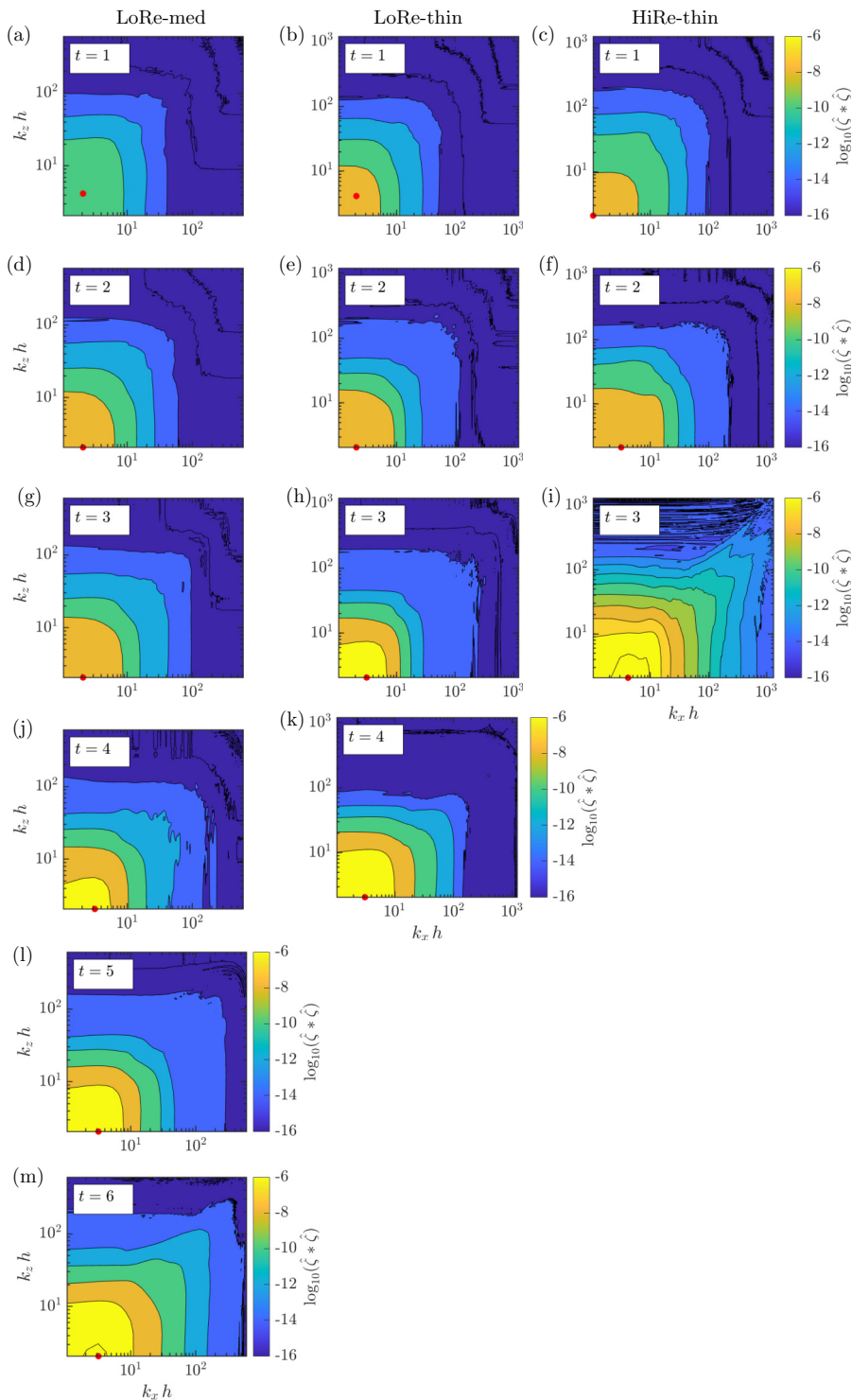
FIG. 7. Spectra of the surface displacement $\zeta$, computed for the same top film surfaces for the same three cases shown in Fig. 6. The maximum in each subfigure is marked with a red bullet.
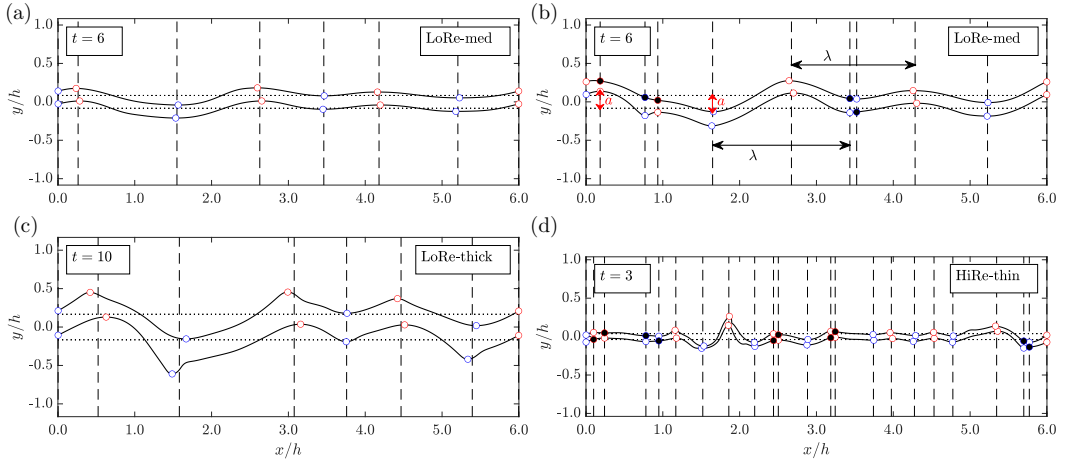
FIG. 8. Indicative division of the deforming film into segments or panels, indicated by the vertical dashed lines, based on local minima and maxima (open bullets); (a, b) samples from the LoRe-med case at $t = 6$ at two different spanwise locations; (c) LoRe-thick case at $t = 10$; (d) HiRe-thin case at $t = 3$. Filled bullets indicate points added from one side of the film to another if absent within a specified tolerance based on the starting film thickness. This procedure is carried out for each spanwise grid location. In some cases [e.g., subfigures (a) and (c)] no additional points need to be added, but in most cases [e.g., subfigures (b) and (d)] they are required in order to deduce the segments for the calculation of $C_{L,\text{cumul.}}$. For the purposes of calculating wavelengths ($\lambda$) and amplitudes ($a$) of the deforming liquid surface, only genuine local extrema (open bullets) are used; sample measurements are marked in (b).

bullets) on either side of the film. The distance between adjacent local minima or maxima is used to deduce a wavelength; since we can record this on either side of the film, we have up to four measurements of the wavelength for each $z$ (spanwise) location. The amplitude is defined as being the distance between the local extrema and the starting flat film location (horizontal dotted lines in Fig. 8). Additional closed bullets are added in order to deduce segments or panels (vertical dashed lines in Fig. 8) for the aerodynamic coefficient calculations in Sec. IV D 2. This was done by checking if minima or maxima found on one side of the film had a corresponding "partner" on the other side of the film within a certain tolerance based on $w_{\ell,0}$. If this was absent, the "orphan" minimum/maximum was copied to the other side of the film.

The procedure demonstrated in Fig. 8 allows us to calculate various parameters of the liquid sheet's deformation. Figure 9 plots the development of the streamwise liquid surface wavelength $\lambda$ and amplitude $a$ in time. Note that significant film deformation must occur to reliably measure $\lambda$ or $a$, therefore the curves in Fig. 9 begin at different $t \geqslant 0$ depending on the film's rate of deformation. Interestingly, $\lambda$ does not vary significantly in time, as shown in Fig. 9(a). Despite their ubiquity, small liquid surface deformations have remained uncharacterized within experiments until recently due to their small size requiring very high surface-normal resolution. In a turbulent wind-driven water wave setup, Ref. [45] found the amplitude of "wrinkles" emerging below the wave threshold to scale with $\sim v_{\ell}^{-1/2} u_{\tau}^{3/2}$, whereas their size (related to the present $\lambda$) remained virtually unchanged. The present simulations are clearly beyond the "wave threshold," yet the early small deformations on the film's surface may be similar to that observed by Ref. [45]. Figure 9(a) suggests that the $\lambda$ that emerges is influenced by both the Reynolds number and the film thickness for the present cases, yet once it emerges, it does not seem to change significantly as the film continues to deform away from the starting film location. Similar to the observations of [10], we find that the scale at which the film ruptures ($\lambda$) is two orders of magnitude larger than the most-amplified wavelength $\lambda \sim \gamma / \rho_g U_{\infty}^2$ suggested by linear theory describing the Squire instability for a fast liquid sheet
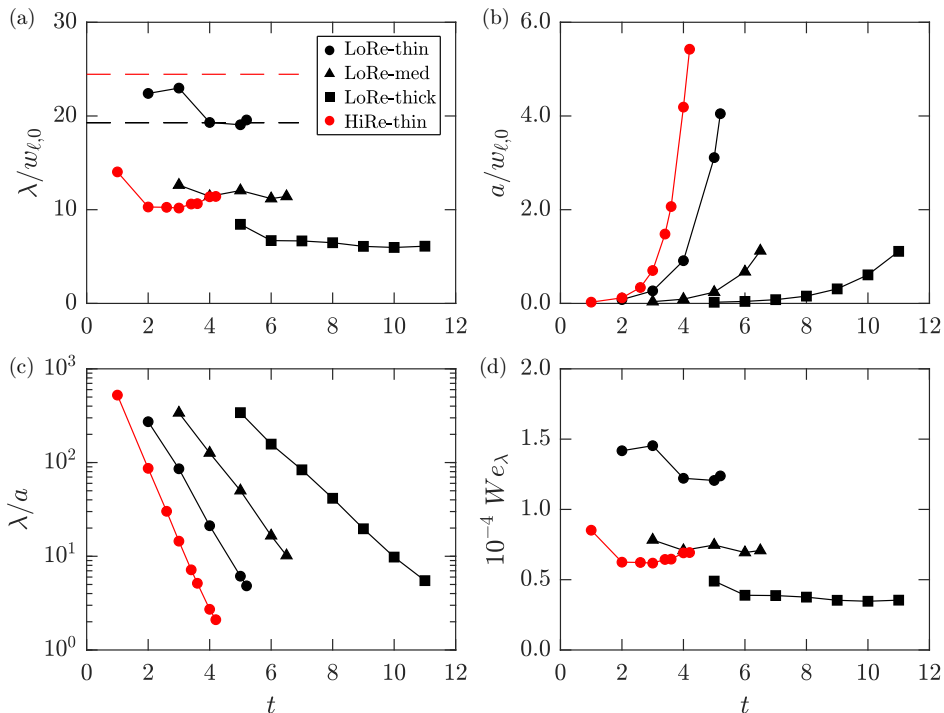
FIG. 9. Characteristics of the deforming film as a function of time; (a) streamwise wavelength of the film's surface $\lambda$; $---$, estimate of the most amplified streamwise wavelength according to linear stability theory using $u_{\tau,0}$ as the velocity scale for the LoRe cases; $---$, same for the HiRe case; (b) amplitude of surface deformation $a$ (measured as the difference from the original film's location on either side); (c) ratio $\lambda/a$; (d) We$_\lambda$, a Weber number defined using $\lambda$, the streamwise wavelength of the deforming film. Note that significant film deformation must occur to reliably measure $\lambda$ or $a$, therefore the curves in Fig. 9 begin at different $t \geqslant 1$ depending on the film's rate of deformation. Symbols as per the legend in (a).

issuing into a lighter environment at rest [4,5], assuming this applies to the present setup via Galilean transformation. However, using $u_{\tau,0}$ as the velocity scale yields a linear-theory estimate of $\lambda$ that is a similar order of magnitude to that measured in the simulations [dashed lines in Fig. 9(a)]. Unlike the wavelength $\lambda$, $a$ increases exponentially with time as shown in Fig. 9(b), which means the ratio $\lambda/a$ decreases exponentially in Fig. 9(c). Reference [47] found breakup of the liquid jet to occur at a ratio of $\lambda/a \approx 2$ in their experimental study. In the present cases, where the curves extend until the film ruptures, we find that the HiRe-thin case (red bullets) achieves a minimum value of $\lambda/a \approx 2$, however in the other cases the film ruptures earlier. The initial Weber number We$_0$ was set to 500 for all the present cases in order to deduce the surface tension coefficient $\gamma$. However, Fig. 9(d) considers an alternate Weber number defined using $\lambda$, the streamwise wavelength of the deforming film [27]:

$$\text{We}_\lambda = \frac{\rho_\ell U_\infty^2 \lambda}{\gamma}, \tag{6}$$

where $\gamma$ is that deduced from We$_0 = 500$. We$_\lambda$ is significantly larger than We$_0$, being in excess of 15 000 for the LoRe-thin case at early times. A higher Weber number means the external inertial forces acting on the liquid sheet are large compared to the restoring surface tension forces. As expected, the higher values of We$_\lambda$ for the LoRe-thin case are consistent with our observations that

the thin film will be more susceptible to deforming inertial forces, and therefore rupture earlier, than the LoRe-med and LoRe-thick cases.

### D. Aerodynamics of film rupture

As discussed in the Introduction, previous studies have suggested the central role of aerodynamic effects in liquid film breakup for a liquid fuel-to-gas density ratio of less than 500 [27], the present ratio being 40. However, the role of the evolving pressure field has not been thoroughly investigated given the experimental difficulty, if not impossibility, of measuring the pressure field in the vicinity of a liquid surface. This section seeks to investigate these suggested aerodynamic processes using an application of classical aerodynamics to quantify the liquid film's deformation and rupture. Our analysis suggests the film's evolution can be broadly understood in terms of inviscid processes, where the liquid film can be effectively understood as a deformable surface until it ruptures.

#### 1. Pressure fluctuations

Figure 10 shows contours of fluctuations in the pressure field over the deforming film. They are shown for the same three cases as in Figs. 3 and 4, but at different times, corresponding to the emergence of significant alternating pressure minima and maxima that directly precedes film rupture. Contours of the film are superimposed highlighting the pressure jump across the gas-liquid interface. While the pressure fluctuations are somewhat weaker in the LoRe-med case [Fig. 10(a)], the pattern of minima and maxima nonetheless looks quite similar to that of the LoRe-thin case [Fig. 10(b)]. We note that this common pattern emerges at an earlier time ($t = 4$) for the LoRe-thin case compared to the LoRe-med case ($t = 5$) because the thicker film delays film deformation and also has a much smaller $\mathrm{We}_\lambda$ [Fig. 9(d)]. For the higher Reynolds number case [Fig. 10(c)], the alternating minima and maxima in the pressure field have a considerably smaller streamwise scale, and a clear alternating pattern emerges earlier at $t = 3$ as is reflected in the smaller and more contorted features seen in Fig. 4. The alternating minima and maxima in the pressure field suggests that each segment of the deforming film can be considered to effectively function as an airfoil, which motivates the analysis below. Reference [48] simulated the flow over a wavy solid surface to study waves of steepness sufficient to induce boundary layer separation and vortex generation in the wind flow, and it considered form drag over the wavy boundaries. In the early stages of the film's deformation, it would seem to share similarities with a wavy water surface. The simulations of Ref. [48] produced similar pressure fields to that shown in the present work for the deforming liquid film.

#### 2. Lift and drag over the deforming film

As mentioned previously, a high Weber number means that the deforming external inertial forces are large compared to the restoring surface tension forces. In the present configuration, the film's breakup is therefore likely to be dominated by aerodynamic effects, including the lift force [2]. Following the insight gained from Fig. 10, we investigate the development of aerodynamic quantities derived from the pressure field, namely the lift and drag coefficients, over the deforming film using a panel methodology applicable up to the point of film rupture.

The total force exerted on the film surface may be calculated from the integral of the stress tensor over the film surface,

$$F_{\text{film}} = \int_\Gamma [(\boldsymbol{\tau} - p\mathbf{I}) \cdot \mathbf{n}] dS, \tag{7}$$

which can be approximated from the VOF field $\phi$ as

$$F_{\text{film}} = \int_V [(\boldsymbol{\tau} - p\mathbf{I}) \cdot \mathbf{n}\, \delta_\Gamma] dV, \tag{8}$$

where $\mathbf{n}\, \delta_\Gamma$ is a regularized Dirac delta function computed as $\nabla\phi$ [36].
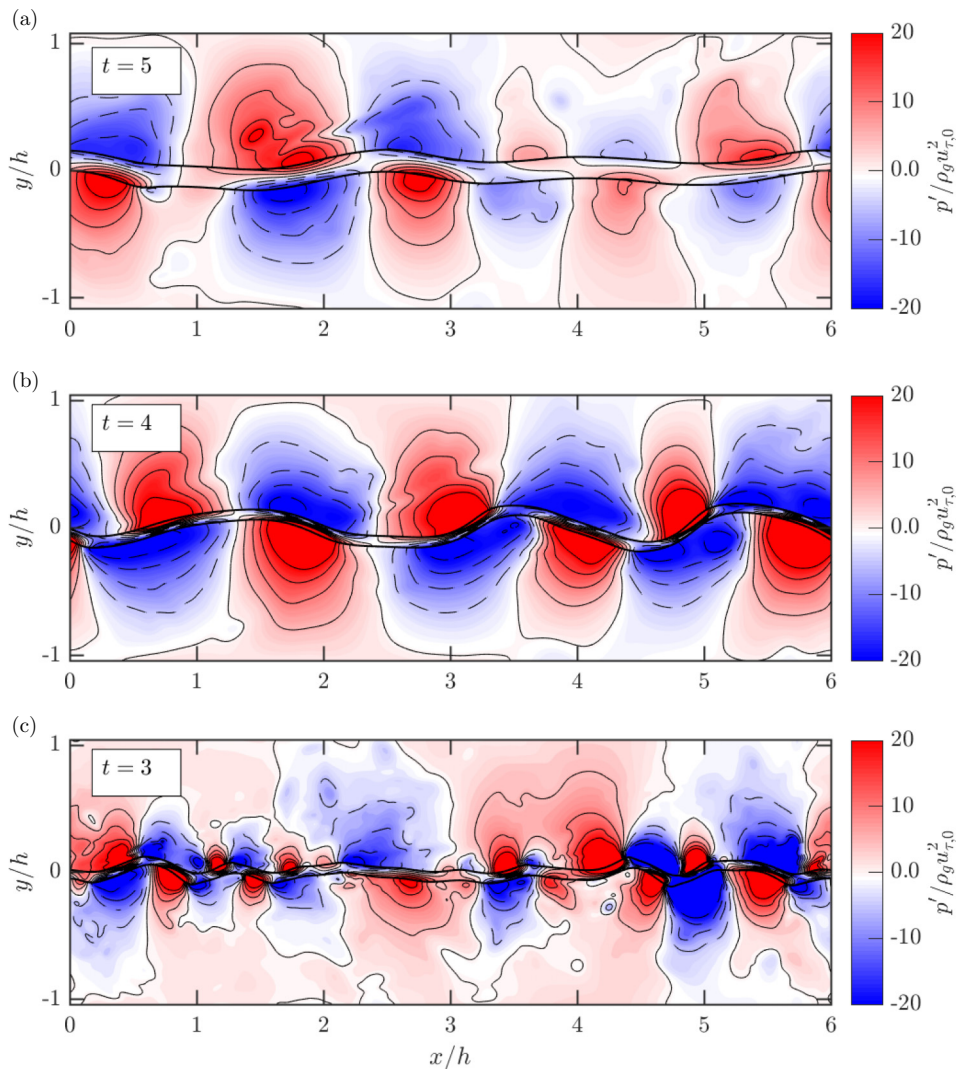
FIG. 10. Indicative contours of the normalized pressure fluctuations over the deforming film for the different cases; contours are spaced at intervals of $5p'/\rho_g u_{\tau,0}^2$: (a) LoRe-med case, with $\mathrm{Re}_{\tau,0} = 180$, $t = 5$; (b) LoRe-thin case with $\mathrm{Re}_{\tau,0} = 180$, $t = 4$; (c) HiRe-thin case with $\mathrm{Re}_{\tau,0} = 393$, $t = 3$. Solid lines denote positive contours and dashed lines negative contours in each case. Thicker black contours denote the surface of the liquid film.

The viscous stress components $F_{\mathrm{film},\mu,i}$ of this force [corresponding to the $\boldsymbol{\tau} \cdot \mathbf{n}\delta_\Gamma$ terms in (8)] are shown in Fig. 11. They are plotted as skin friction drag coefficients [i.e., $C_{\mu,x} = 2F_{\mathrm{film},\mu,x}/(\rho_g U_\infty^2 A_{\mathrm{film}})$] to permit comparison to the drag and lift coefficients plotted in Fig. 12. All three viscous components are much smaller than the inviscid pressure components, with only the $x$-component non-negligible. The value of $C_{\mu,x}$ in Fig. 11(a) is set by the Reynolds number of the gas flow, therefore that of the HiRe-thin case is slightly higher than that of all other cases. This force tends toward zero with time as the mean shear profile decays over the duration of the simulations [cf., Figs. 5(d)–5(f)]. Overall, these plots confirm the minor role of parasitic drag in the
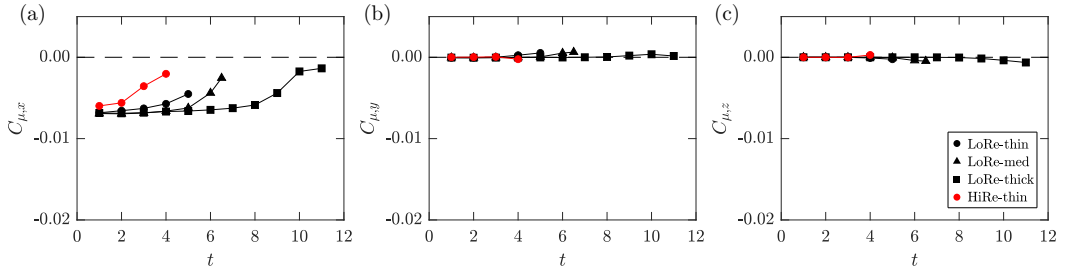
FIG. 11. Viscous stress over the deforming film plotted as skin friction drag coefficients, analogous to Fig. 12 (note the extent of the vertical axis of these plots is only 1/10th that of the plots in Fig. 12); (a) streamwise $x$ component; (b) film-normal $y$ component; (c) spanwise $z$ component. Symbols as per legend in (c).

current simulations, and we therefore focus on the role of the inviscid forces, namely the lift and lift-induced drag, on the deformation and rupture of the liquid film.

For this section, we make use of the segments shown in Fig. 8. Calculating the lift over the entire film is statistically zero since the problem is symmetric in the film-normal direction (i.e., vertical forces resulting from adjacent, vertically alternating, pressure minima-maxima pairs cancel when integrated over the entire film). However, it is clear from Fig. 10 that there is a local segmentwise lift serving to increasingly deform the film. The lift-induced drag ($F_{D,p}$) and lift ($F_L$) forces are defined
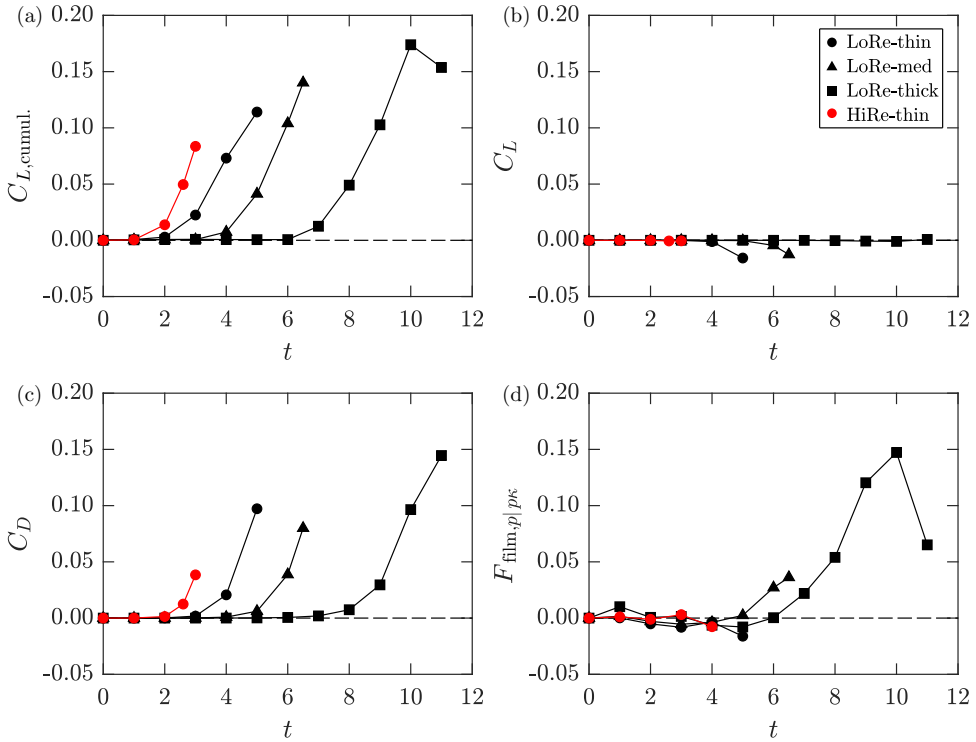


FIG. 12. Aerodynamic coefficients over the deforming film for the different cases. Symbols as per the legend in (b).

as

$$F_{D,p} = \int p\,\mathbf{n} \cdot \mathbf{i}\,dS, \quad F_L = \int p\,\mathbf{n} \cdot \mathbf{j}\,dS, \tag{9}$$

where $\mathbf{n}$ is the inward pointing normal vector to the film's surface, $\mathbf{i}$ is the unit normal vector in the streamwise $x$ direction, $\mathbf{j}$ is the unit normal vector film-normal direction $y$, and $dS$ is the elemental surface area of the film. Throughout, this analysis has been performed at each spanwise location. Figure 12(a) shows the segmentwise "cumulative" lift coefficient $C_{L,\mathrm{cumul.}} = 2F_{L,\mathrm{cumul.}}/(\rho_g U_\infty^2 A_{\mathrm{film}})$, which is seen to increase steeply with time as the film deforms in the different cases, pointing to the central role of pressure in amplifying film deformation. The cumulative lift force $F_{L,\mathrm{cumul.}}$ is defined as the sum of the absolute values of the lift force $F_L$ on each segment of the film, $U_\infty$ is in this case the (decaying) mean streamwise velocity, and $A_{\mathrm{film}}$ is the deforming film's surface area. As expected, Fig. 12(b) shows that the typical lift coefficient $C_L = 2F_L/(\rho_g U_\infty^2 A_{\mathrm{film}})$ is zero during the simulations, illustrating that the lift felt by each individual panel is canceled out with that of its neighbor. The action of the lift force is therefore hidden if the lift analysis is not carried out using a panel method approach. Exponential growth in $C_{L,\mathrm{cumul.}}$ is observed in the different cases, with all curves ending when the film's surface is no longer intact, since at that point the pressure integration over the film's surface is no longer well-defined. Interestingly, $C_{L,\mathrm{cumul.}}$ is shown to decrease at late times just before the film ruptures for the LoRe-thick case. Integration of the $-p\mathbf{I} \cdot \nabla\phi$ term in (8) yields plots virtually identical to Figs. 12(b) and 12(c), meaning that the contribution of the stress tensor on the liquid side to the net force on the film, a contribution omitted in the lift and drag calculated using the external pressure according to (9), is much smaller than that on the gas side. The drag coefficient over the deforming film is defined as $C_D = 2F_{D,p}/(\rho_g U_\infty^2 A_{\mathrm{film}})$, where $F_{D,p}$ is the lift-induced drag force over both surfaces of the film. Figure 12(c) shows how $C_D$ develops in time for the present cases. $C_D$, calculated over the entire film, develops in a similar manner to the panelwise $C_{L,\mathrm{cumul.}}$. The drastic increase in the lift-induced drag coefficient as the film deforms compared to the small, and relatively stable, values of the parasitic drag coefficient (Fig. 11) again points to the dominance of lift-induced drag and the minor role of parasitic drag. The increasing lift-induced drag and cumulative lift coefficients over the film as it deforms appear to scale consistently with film thickness and therefore may provide a useful means for ultimately predicting the time to film rupture.

We now consider the inviscid pressure component of (8), $F_{\mathrm{film},p}$, conditioned on the local curvature $\kappa$:

$$F_{\mathrm{film},p|p\kappa} = \int_V \{[p\mathbf{I} \cdot \mathbf{n}]|(p\kappa) < 0\}dV. \tag{10}$$

This quantity attempts to capture the amplification of deformation in the film's surface due to the pressure field, and we will consider here the film-normal $y$ component. If the curvature has the opposite sign of the $y$-component of $F_{\mathrm{film},p}$ (i.e., like pressing down on the inside of a parabola), then the lift force will tend to deform the film further. If it is of the same sign as the curvature, the lift force will tend to reduce the curvature of the film's surface. Figure 12(d) shows the vertical component of the conditioned inviscid vertical force. It follows the values of $C_{L,\mathrm{cumul.}}$ for the LoRe-thick film case quite closely until $t = 10$. It also increases at late times for the LoRe-med case, although it remains significantly smaller than $C_{L,\mathrm{cumul.}}$. It is less effective as a measure of the action of the lift force for the thin film cases.

The cumulative lift force $C_{L,\mathrm{cumul.}}$ captures the emerging pressure minima and maxima forming on the film surface, which results in film rupture. We now seek to collapse the temporal development of $C_{L,\mathrm{cumul.}}$ [Fig. 12(a)] for the different cases. Scaling time with the bulk velocity $U_{b,0}$ and starting film thickness $w_{\ell,0}$ does not appear to collapse the late-time development of $C_{L,\mathrm{cumul.}}$ [Fig. 13(b)], although the start of the steep increase in $C_{L,\mathrm{cumul.}}$ occurs at $t^* = tU_{b,0}/w_{\ell,0} \approx 40$ for all the cases. As the boundary layer over each panel varies, an alternate velocity scale $u_{\tau,D}$ is calculated from the lift-induced drag force $F_{D,p}$, where $F_{D,p}$ is plotted in the form of a drag coefficient $C_D$ in Fig. 12(c).
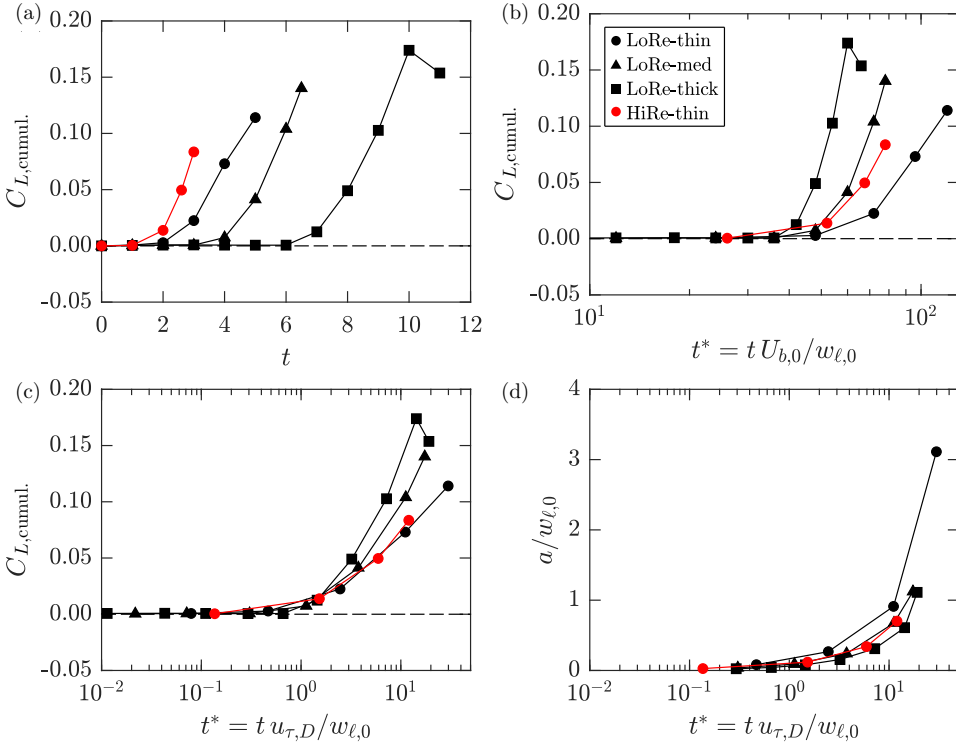
FIG. 13. (a) Cumulative lift coefficient $C_{L,\mathrm{cumul.}}$ [same as Fig. 12(a)]; (b) temporal development of $C_{L,\mathrm{cumul.}}$ scaled with $t^*$ formed from the starting bulk velocity $U_{b,0}$ and the starting film thickness $w_{\ell,0}$; (c) temporal development of $C_{L,\mathrm{cumul.}}$ scaled with $t^*$ formed from $u_{\tau,D}$, a friction velocity derived from the lift-induced drag force $F_{D,p}$ and $w_{\ell,0}$; (d) amplitude of film deformation scaled with $w_{\ell,0}$, measured as a deviation from the original film surface location [Fig. 9(b)], plotted against the scaled time $t^*$ formed from $u_{\tau,D}$ and $w_{\ell,0}$ as in (c). Symbols as per the legend in (b).

We define this velocity scale as

$$u_{\tau,D} = \sqrt{\frac{F_{D,p}}{\rho_g A_{\mathrm{film}}}}. \tag{11}$$

This velocity scale can be interpreted as a kind of mean streamwise inertial force over the film. Against logarithmic horizontal scales, $u_{\tau,D}$ collapses both $C_{L,\mathrm{cumul.}}$ and the film's amplitude with some success, even at late times [Figs. 13(c) and 13(d)], noting that $u_{\tau,D}$ is only defined so long as the film's surface remains intact.

### 3. Flow reversal

Deformations of large enough amplitude are accompanied by flow reversal as the gas-phase turbulent boundary layer separates from the liquid film surface, as reported in [23]. Figure 14 shows the percentage of reversed flow for the different cases as a function of time. As the film deforms, low pressure regions form (Fig. 10) correlating with recirculation of the flow (white regions in Fig. 4). Significant flow reversal only appears to occur directly before the film ruptures, suggesting its role in this process. The LoRe-thick case can withstand a much larger percentage of reversed flow than the other cases. The total area of the film's surface is shown in Fig. 14(b). The area's increase in time
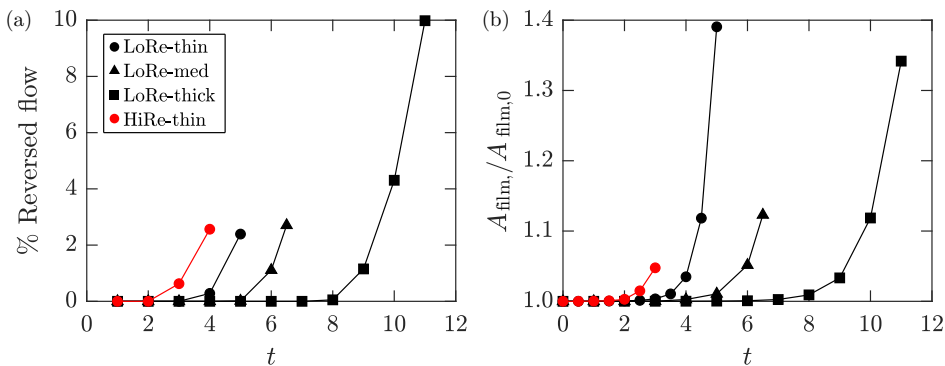
FIG. 14. (a) Percentage of reversed flow in time; (b) increasing total film surface area with time. Symbols as per the legend in (a).

appears to closely follow that of the percentage of reversed flow of Fig. 14(a) with the exception of a much higher relative value of the film's area at $t = 5$ for the LoRe-thin case.

### 4. Impulse on the liquid sheet: Linking pressure to film displacement

The pressure impulse theory for incompressible liquid impact problems was described in Ref. [49] as an inviscid process where the pressure impulse is $P(x, y, z, t) = \int_{t_b}^{t_a} p(x, y, z, t) dt$ for times $t_a$ and $t_b$ immediately before and after "impact." In the present work, the "impact" refers to the largely inviscid action of the gas phase on the quiescent liquid film. $P$ is related to the change in momentum of the liquid phase as

$$(\mathbf{u}_{\ell,a} - \mathbf{u}_{\ell,b})\rho_\ell = -\boldsymbol{\nabla}P, \qquad (12)$$

where $\mathbf{u}_{\ell,a} = u_\ell(x, y, z, t_a)$ and $\mathbf{u}_{\ell,b} = u_\ell(x, y, z, t_b)$ are the velocities of the liquid film phase at times $t_a$ and $t_b$. Since the liquid film is initially at rest, in the present context the integrated pressure impulse at any given time is equal to the momentum of the liquid phase. Figure 15 plots the momentum of the liquid film in time (i.e., between the contours marking the top and bottom surface of the film, as shown in Fig. 8). Both subfigures in Fig. 15 plot the sum of the absolute value in the change of
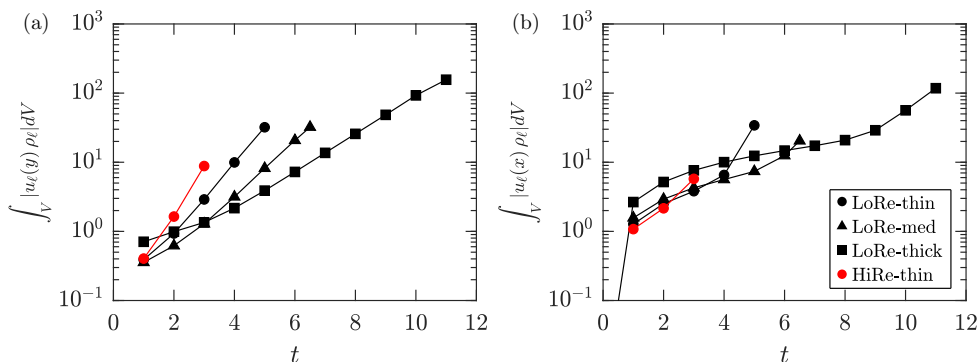


FIG. 15. Impulse on the liquid film over time (change in momentum); (a) film-normal impulse; (b) streamwise impulse. Symbols as per the legend in (b).

TABLE III. Parameters for the companion thin liquid film simulations. Subscript "0" refers to parameters at the instant the film simulations are started. Fully developed turbulent velocity fields from the channel simulations (Table I) form the gas phase; $\mathrm{Re}_{\tau,0}$ refers to the Reynolds number of this gas phase. The viscous-scaled initial film thickness is $w_{\ell,0}^+ = \mathrm{Re}_{\tau,0}(w_{\ell,0}/h)$. Both simulations have domain size $L_x/h = 6$, $L_y/h = 2 + w_{\ell,0}$, and $L_z/h = 3$.

| Case name | Symbol | $\mathrm{Re}_{\tau,0}$ | $w_{\ell,0}/h$ | $w_{\ell,0}^+$ | $N_x$ | $(N_{\ell,y})_0$ | $N_y$ | $N_z$ | $(\Delta x^+)_0$ | $(\Delta y^+)_0$ | $(\Delta z^+)_0$ |
|---|---|---|---|---|---|---|---|---|---|---|---|
| LoRe-thin | ● | 180 | 1/12 | 15.0 | 2304 | 32 | 800 | 1152 | 0.47 | 0.47 | 0.47 |
| LoRe-thin-loRes | ● | 180 | 1/12 | 15.0 | 1152 | 16 | 400 | 576 | 0.94 | 0.94 | 0.94 |

momentum within the film calculated for each panel. Similar to the lift coefficient, the change in the $y$-momentum (film-normal direction) would be statistically zero if the panel methodology were not used. Figure 15(a) shows that the change in $y$-momentum grows exponentially in time in a similar manner to the cumulative lift coefficient [Fig. 12(a)] and lift-induced drag coefficient [Fig. 12(c)]. In contrast, there is a more steady growth in the change of $x$-momentum (streamwise direction), with more similar behavior for the different cases at early times. Note the uptick in the $x$-momentum seen for all the cases at late times. This results from the large emerging film deformations causing large changes in the streamwise flow, including flow reversal. For example, this occurs by $t \approx 3$ for the HiRe-thin case, but it does not occur until $t \approx 9$ for the LoRe-thick case. This points to different origins in the change in momentum in the different directions: a change in $y$-momentum can only occur if the film deforms since the problem is symmetric. In contrast, even a film that is not deforming will have $x$-momentum imparted to it by the "dragging" motion of the coflowing gas-phase boundary layers on either side of it.
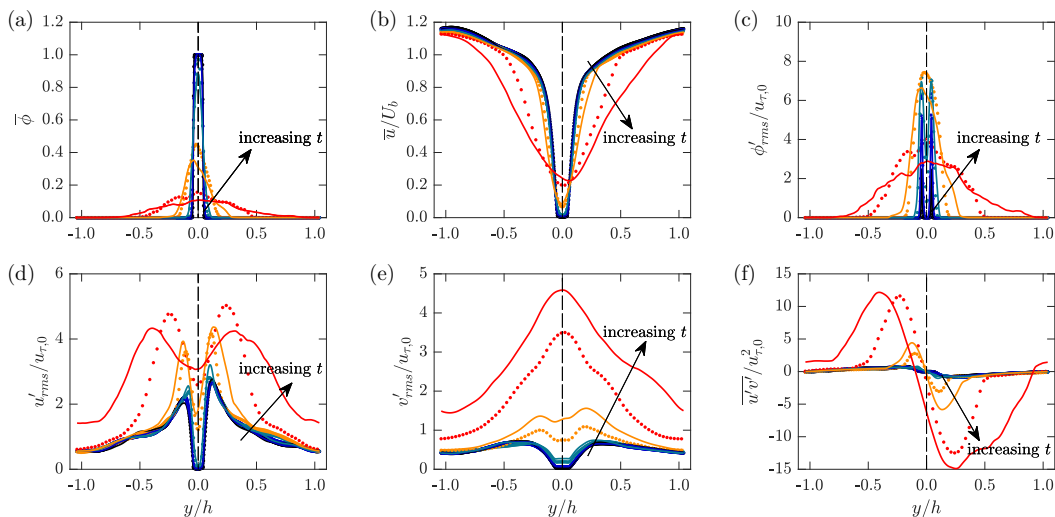


FIG. 16. Comparing the temporal development of statistics averaged in the homogeneous $xz$-planes for the thin film at two different simulation grid resolutions; bullets, LoRe-thin case (same as in Fig. 5); lines, LoRe-thin-loRes case. Curves colored by time: ——, $t = 1$; ——, $t = 2$; ——, $t = 3$; ——, $t = 4$; ——, $t = 5$; – – –, domain centerline.
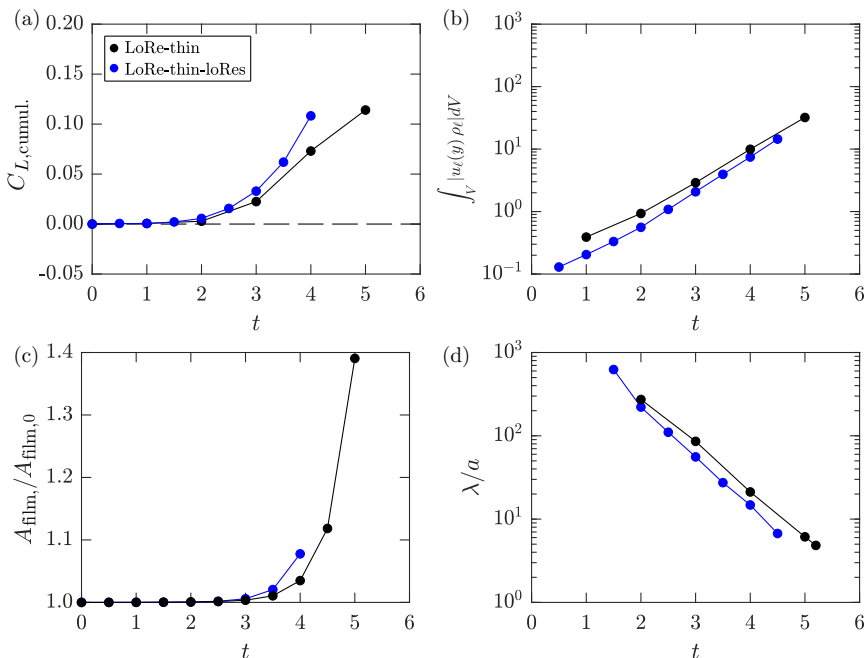
FIG. 17. Comparing the temporal development of bulk quantities for the thin film at two different simulation grid resolutions. Symbols as per the legend in (a).

## V. CONCLUSIONS

The aerodynamically driven rupture of a liquid film has been simulated using a VOF method. The present results demonstrate the utility of this numerical setup, utilizing realistic fully developed turbulent gas-phase shear layers from a channel simulations, to parametrically investigate the role of important physical parameters such as film thickness and gas-phase Reynolds number in liquid film deformation and rupture. Aligning with the results of Ref. [26], the presence of more, and smaller, turbulent scales at the higher Reynolds number considered here hastens film rupture. Rupture of the liquid sheet appears to occur due to the amplification of aerodynamic lift over segments of the deforming film, at a scale much larger than instabilities predicted by linear stability analysis. A cumulative lift force is introduced to capture the alternating pressure minima and maxima forming over the film, which amplify to eventually rupture the film. A velocity scale derived from the lift-induced drag force collapses the development of this cumulative lift force as well as the amplitude of film deformation with some success for the different film thicknesses and Reynolds numbers considered in the present work. This setup will be used in future simulation campaigns building on the present "cold" simulations to study the transfer of heat and species via deforming and moving gas-liquid interfaces to understand ensuing interfacial thermodynamics within a turbulent environment.

**APPENDIX: RESOLUTION OF THE THIN-FILM CASE**

The thin-film case is simulated at two different resolutions (Table III), the effect of which is considered here. The LoRe-thin case is that presented in the main body of the paper, and here we consider another lower resolution of the same physical setup named LoRe-thin-loRes, which has the same starting grid resolution as the LoRe-med, LoRe-thick, and HiRe-thin cases of Table II. The two thin-film cases are shown here to broadly evolve in a similar manner. Some of the differences between the two cases may be due to the fact that the present simulations are only modestly statistically converged, since the current dataset relies on single realizations of each case.

Figure 16 compares the temporal development of the LoRe-thin and LoRe-thin-loRes cases, reproducing the plots of Fig. 5. There is some disagreement at late times, however the curves at specific times are overall similar, especially in the context of the large differences found between the cases differing in film thickness and Reynolds number in Fig. 5. Larger differences are found for second-order statistics [Figs. 17(d)–17(f)] at later times ($t = 4$ and 5), where $t = 5$ is approximately the time the film ruptures. More uncertainty is expected upon film rupture, since for the present VOF method topology changes take place (primarily occurring due to local film rupture or thread breaking) when the resolution of a film or thread is sufficiently low [51], meaning the size of the liquid structure approaches that of the grid size.

Figure 17 compares the temporal development of bulk quantities for the LoRe-thin and LoRe-thin-loRes cases. Small discrepancies are found for late times ($t = 4$ onward) when the LoRe-thin-loRes has already begun to rupture due to fine structures reaching the size of the grid spacing triggering a change in topology. Nevertheless, good agreement is found for the two cases.

---

[1] A. H. Lefebvre and D. R. Ballal, *Gas Turbine Combustion: Alternative Fuels and Emissions* (CRC, Boca Raton, FL. 2010).

[2] O. Desjardins and H. Pitsch, Detailed numerical investigation of turbulent atomization of liquid jets, Atom. Sprays **20**, 311 (2010).

[3] M. Aigner and S. Wittig, Swirl and counterswirl effects in prefilming airblast atomizers, J. Eng. Gas Turb. Power **110**, 105 (1988).

[4] H. B. Squire, Investigation of the instability of a moving liquid film, Br. J. Appl. Phys. **4**, 167 (1953).

[5] E. Villermaux, Fragmentation versus cohesion, J. Fluid Mech. **898**, P1 (2020).

[6] R. H. Rangel and W. A. Sirignano, The linear and nonlinear shear instability of a fluid sheet, Phys. Fluids **3**, 2392 (1991).

[7] X. Li and R. S. Tankin, On the temporal instability of a two-dimensional viscous liquid sheet, J. Fluid Mech. **226**, 425 (1991).

[8] A. Lozano, F. Barreras, G. Hauke, and C. Dopazo, Longitudinal instabilities in an air-blasted liquid sheet, J. Fluid Mech. **437**, 143 (2001).

[9] T. Otto, M. Rossi, and T. Boeck, Viscous instability of a sheared liquid-gas interface: Dependence on fluid properties and basic velocity profile, Phys. Fluids **25**, 032103 (2013).

[10] S. S. Deshpande, S. R. Gurjar, and M. F. Trujillo, A computational study of an atomizing liquid sheet, Phys. Fluids **27**, 082108 (2015).

[11] P. Marmottant and E. Villermaux, On spray formation, J. Fluid Mech. **498**, 73 (2004).

[12] A. Agarwal and M. F. Trujillo, A closer look at linear stability theory in modeling spray atomization, Int. J. Multiphase Flow **109**, 1 (2018).

[13] I. S. Carvalho and M. V. Heitor, Liquid film break-up in a model of a prefilming airblast nozzle, Exp. Fluids **24**, 408 (1998).

[14] A. Mansour and N. Chigier, Dynamic behavior of liquid sheets, Phys. Fluids A **3**, 2971 (1991).

[15] O. Tammisola, A. Sasaki, F. Lundell, M. Matsubara, and L. D. Söderberg, Stabilizing effect of surrounding gas flow on a plane liquid sheet, J. Fluid Mech. **672**, 5 (2011).

[16] S. Gepperth, D. Guildenbecher, R. Koch, and H.-J. Bauer in *Proceedings of the 23rd Annual Conference on Liquid Atomization and Spray Systems* (ILASS–Europe, Naples, Italy, 2010).

[17] D. Duke, D. Honnery, and J. Soria, Experimental investigation of nonlinear instabilities in annular liquid sheets, J. Fluid Mech. **691**, 594 (2012).

[18] G. Chaussonnet, S. Gepperth, S. Holz, R. Koch, and H.-J. Bauer, Influence of the ambient pressure on the liquid accumulation and on the primary spray in prefilming airblast atomization, Int. J. Multiphase Flow **125**, 103229 (2020).

[19] B. Déjean, P. Berthoumieu, and P. Gajan, Experimental study on the influence of liquid and air boundary conditions on a planar air-blasted liquid sheet, part II: prefilming zone length, Int. J. Multiphase Flow **79**, 214 (2016).

[20] U. Shavit, Gas-liquid interaction in the liquid breakup region of twin-fluid atomization, Exp. Fluids **31**, 550 (2001).

[21] A. Kourmatzis and A. R. Masri, Air-assisted atomization of liquid jets in varying levels of turbulence, J. Fluid Mech. **764**, 95 (2015).

[22] J. Park, K. Y. Huh, X. Li, and M. Renksizbulut, Experimental investigation on cellular breakup of a planar liquid sheet from an air-blast nozzle, Phys. Fluids **16**, 625 (2004).

[23] Y. Ling, D. Fuster, G. Tryggvason, and S. Zaleski, A two-phase mixing layer between parallel gas and liquid streams: Multiphase turbulence statistics and influence of interfacial instability, J. Fluid Mech. **859**, 268 (2019).

[24] D. Jiang and Y. Ling, Destabilization of a planar liquid stream by a co-flowing turbulent gas stream, Int. J. Multiphase Flow **122**, 103121 (2020).

[25] D. Zuzio, J.-L. Estivalèzes, and B. DiPierro, An improved multiscale Eulerian-Lagrangian method for simulation of atomization process, Comput. Fluids **176**, 285 (2018).

[26] K. Warncke, A. Sadiki, and J. Janicka in *Proceedings of the 29th Conference on Liquid Atomization and Spray Systems* (ILASS–Europe, Naples, Italy, 2019).

[27] P. K. Wu and G. M. Faeth, Aerodynamic effects on primary breakup of turbulent liquids, Atom. Sprays **3**, 265 (1993).

[28] S. Ii, K. Sugiyama, S. Takeuchi, S. Takagi, Y. Matsumoto, and F. Xiao, An interface capturing method with a continuous function: The THINC method with multi-dimensional reconstruction, J. Comput. Phys. **231**, 2328 (2012).

[29] A. Zandian, W. A. Sirignano, and F. Hussain, Understanding liquid-jet atomization cascades via vortex dynamics, J. Fluid Mech. **843**, 293 (2018).

[30] A. Lozano, A. Garcıa-Olivares, and C. Dopazo, The instability growth leading to a liquid sheet breakup, Phys. Fluids **10**, 2188 (1998).

[31] P. Trontin, S. Vincent, J. L. Estivalezes, and J. P. Caltagirone, Direct numerical simulation of a freely decaying turbulent interfacial flow, Int. J. Multiphase Flow **36**, 891 (2010).

[32] M. E. Rosti, F. De Vita, and L. Brandt, Numerical simulations of emulsions in shear flows, Acta Mech. **230**, 667 (2019).

[33] J. U. Brackbill, D. B. Kothe, and C. Zemach, A continuum method for modeling surface tension, J. Comput. Phys. **100**, 335 (1992).

[34] P. Costa, A FFT-based finite-difference solver for massively-parallel direct numerical simulations of turbulent flows, Comput. Math. Appl. **76**, 1853 (2018).

[35] D. Fuster, J. P. Matas, S. Marty, S. Popinet, J. Hoepffner, A. Cartellier, and S. Zaleski, Instability regimes in the primary breakup region of planar coflowing sheets, J. Fluid Mech. **736**, 150 (2013).

[36] G. Tryggvason, R. Scardovelli, and S. Zaleski, *Direct Numerical Simulations of Gas-liquid Multiphase Flows* (Cambridge University Press, Cambridge, 2011).

[37] M. Kang, R. P. Fedkiw, and X.-D. Liu, A boundary condition capturing method for multiphase incompressible flow, J. Sci. Comput. **15**, 323 (2000).

[38] K. A. Sallam, C. Aalburg, and G. M. Faeth, Breakup of round nonturbulent liquid jets in gaseous crossflow, AIAA J. **42**, 2529 (2004).

[39] N. Bremond, C. Clanet, and E. Villermaux, Atomization of undulating liquid sheets, J. Fluid Mech. **585**, 421 (2007).

[40] H. Lhuissier and E. Villermaux, Crumpled water bells, J. Fluid Mech. **693**, 508 (2012).

[41] A. Lozano and F. Barreras, Experimental study of the gas flow in an air-blasted liquid sheet, Exp. Fluids **31**, 367 (2001).

[42] G. Agbaglah, R. Chiodi, and O. Desjardins, Numerical simulation of the initial destabilization of an air-blasted liquid layer, J. Fluid Mech. **812**, 1024 (2017).

[43] S. Perrard, A. Lozano-Durán, M. Rabaud, M. Benzaquen, and F. Moisy, Turbulent windprint on a liquid surface, J. Fluid Mech. **873**, 1020 (2019).

[44] N. Scapin, P. Costa, and L. Brandt, A volume-of-fluid method for interface-resolved simulations of phase-changing two-fluid flows, J. Comput. Phys. **407**, 109251 (2020).

[45] A. Paquier, F. Moisy, and M. Rabaud, Viscosity effects in wind wave generation, Phys. Rev. Fluids **1**, 083901 (2016).

[46] M.-Y. Lin, C.-H. Moeng, W.-T. Tsai, P. P. Sullivan, and S. E. Belcher, Direct numerical simulation of wind-wave generation processes, J. Fluid Mech. **616**, 1 (2008).

[47] G. Singh, A. Kourmatzis, A. Gutteridge, and A. R. Masri, Instability growth and fragment formation in air assisted atomization A29, J. Fluid Mech. **892** (2020).

[48] D. Yang and L. Shen, Direct-simulation-based study of turbulent flow over various waving boundaries, J. Fluid Mech. **650**, 131 (2010).

[49] M. J. Cooker and D. H. Peregrine, Pressure-impulse theory for liquid impact problems, J. Fluid Mech. **297**, 193 (1995).

[50] M. Själander, M. Jahre, G. Tufte, and N. Reissmann, EPIC: An energy-efficient, high-performance GPGPU computing research infrastructure, arXiv:1912.05848 [cs.DC].

[51] J. Lu and G. Tryggvason, Multifluid flows in a vertical channel undergoing topology changes: Effect of void fraction, Phys. Rev. Fluids **4**, 084301 (2019).